Improvement from the satellite-derived NO_X emissions on air quality modeling and its effect on ozone and secondary inorganic aerosol formation in Yangtze River Delta, China

Yang Yang[1,5], Yu Zhao[1,2*], Lei Zhang[1], Jie Zhang[3], Xin Huang [4], Xuefen Zhao[1],
Yan Zhang[1], Mengxiao Xi[1] and Yi Lu[1]

1. State Key Laboratory of Pollution Control & Resource Reuse and School of the Environment, Nanjing University, 163 Xianlin Ave., Nanjing, Jiangsu 210023, China

2. Jiangsu Collaborative Innovation Center of Atmospheric Environment and Equipment Technology (CICAEET), Nanjing University of Information Science & Technology, Jiangsu 210044, China

3. Jiangsu Provincial Academy of Environmental Science, 176 North Jiangdong Rd., Nanjing, Jiangsu 210036, China

4. School of the Atmospheric Sciences, Nanjing University, 163 Xianlin Ave., Nanjing, Jiangsu 210023, China

5. College of Environmental & Resource Sciences, Zhejiang University, Hangzhou, Zhejiang 310058, China

*Corresponding author: Yu Zhao

Phone: 86-25-89680650; email: yuzhao@nju.edu.cn

Abstract

We developed a "top-down" methodology combining the inversed chemistry transport modeling and satellite-derived tropospheric vertical column of NO_2, and estimated the NO_X emissions of Yangtze River Delta (YRD) region at a horizontal resolution of 9 km for January, April, July and October 2016. The effect of the top-down emission estimation on air quality modeling, and the response of ambient ozone (O_3) and inorganic aerosols (SO_4^{2-}, NO_3^-, and NH_4^+, SNA) to the changed precursor emissions were evaluated with the Community Multi-scale Air Quality (CMAQ) system. The top-down estimates of NO_X emissions were smaller than those in a national emission inventory, MEIC (i.e., the "bottom-up" estimates), for all the four months, and the monthly mean was calculated at 260.0 Gg/month, 24% less than the bottom-up one. The NO_2 concentrations simulated with the bottom-up estimate of NO_X emissions were clearly higher than the ground observation, indicating the possible overestimation in current emission inventory attributed to its insufficient consideration of recent emission control in the region. The model performance based on top-down estimate was much better, and the biggest change was found for July with the normalized mean bias (NMB) and normalized mean error (NME) reduced from 111% to -0.4% and from 111% to 33%, respectively. The results demonstrate the improvement of NO_X emission estimation with the nonlinear inversed modeling and satellite observation constraint. With the smaller NO_X emissions in the top-down estimate than the bottom-up one, the elevated concentrations of ambient O_3 were simulated for most YRD and they were closer to observation except for July, implying the VOC (volatile organic compound)-limit regime of O_3 formation. With available ground observations of SNA in the YRD, moreover, better model performance of NO_3^- and NH_4^+ were achieved for most seasons, implying the effectiveness of precursor emission estimation on the simulation of secondary inorganic aerosols. Through the sensitivity analysis of O_3 formation for April 2016, the decreased O_3 concentrations were found for most YRD region when only VOCs emissions were reduced or the reduced rate of VOCs emissions was two times of that of NO_X, implying the crucial role of VOCs control on O_3 pollution abatement. The SNA level for January 2016 was simulated to decline 12% when 30% of NH_3 emissions were reduced, while the change was much smaller with the same reduced rate for SO_2 or NO_X. The result suggests that reducing NH_3 emissions was the most effective way to alleviate SNA pollution for YRD in winter.

1. Introduction

Nitrogen oxides ($NO_X = NO_2 + NO$) play an important role on the formation of ambient ozone (O_3) and inorganic aerosols (SO_4^{2-}, NO_3^-, and NH_4^+, SNA). The NO_X emission inventory is a necessary input of the air quality model (AQM), and has a great influence on NO_2, O_3 and SNA simulation (Zhou et al., 2017; Chen et al., 2019a). Moreover, it is crucial for exploring the sources of atmospheric pollution of O_3 and fine particles (particles with aerodynamic diameter smaller than 2.5μm, $PM_{2.5}$) with AQM. The inventories were usually developed with a bottom-up method, in which the emissions were calculated based on the activity data (e.g., fuel consumption and industrial production) and emission factors (the emissions per unit of activity data) by source category and region. Bias existed commonly in the bottom-up inventories, due mainly to the uncertainty of economic and energy statistics and to the fast changes in the emission control measures, especially in developing countries like China (Granier et al., 2011; Saikawa et al., 2017; Zhang et al., 2019).

To improve the emission estimation, an inversed “top-down” method has been developed based on satellite observation and AQM (Martin et al., 2003; Zhao and Wang, 2009; Zyrichidou et al., 2015; Yang et al., 2019a). The emissions were corrected based on the difference between the modeled and observed tropospheric vertical column densities (TVCDs) of NO_2, and the response coefficient of NO_2 TVCDs to emissions (Martin et al., 2003; Cooper et al., 2017). With higher temporal and spatial resolution than other instruments, the NO_2 TVCDs from Ozone Monitoring Instrument (OMI) were frequently used (Kurokawa et al., 2009; Gu et al., 2014; de Foy et al., 2015; Kong et al., 2019; Yang et al., 2019a).

Currently, the top-down methods were mainly developed at the global or national scale with relatively coarse horizontal resolution (Martin et al., 2003; Miyazaki et al., 2012; Jena et al., 2014; Gu et al., 2014). At the global scale, for example, Martin et al. (2003) and Miyazaki et al. (2012) estimated the NO_X emissions at the horizontal resolution of 2°×2.5° and 2.8°×2.8°, respectively. Martin et al. (2003) found that the satellite-derived NO_X emissions for 1996-1997 were 50-100% larger than the bottom-up estimates in the Po Valley, Tehran, and Riyadh urban areas. Miyazaki et al. (2012) suggested that the bottom-up method underestimated the NO_X emissions over eastern China, eastern United States, southern Africa, and central-western Europe. At the national scale with the horizontal resolution of 0.5°×0.5°, the annual NO_X emissions in India 2015 derived with the top-down method was 7-60% smaller than various bottom-up estimates (Jena et al., 2014). With the TVCDs from OMI and another instrument (Global Ozone Monitoring Experiment, GOME), the difference in national NO_X emissions for China was quantified at 0.4 Tg N/yr (5.8% relative to OMI) at the resolution of 70×70 km (Gu et al., 2014). Compared to national and regional ones, limited estimates were available at the regional scale with finer resolution. In China, great differences exist in the levels and patterns of air pollution across the regions, attributed partly to a big variety of air pollutant sources across the country. To achieve the target of air quality improvement required by the central government, varied air pollution control plans were usually developed and implemented at the city/provincial levels. Therefore, the top-down estimates in NO_X emissions at finer horizontal resolution are in great need for understanding the primary sources of NO_2 pollution and demonstrating the effect of emission control at the regional scale.

At present, the reliability and rationality of the top-down emission estimates were commonly evaluated with AQM and satellite observation. For example, the bias between the NO_2 TVCDs from OMI observation and AQM based on the top-down NO_X emission estimation was $-30.8\pm69.6\times10^{13}$ molecules cm^{-2} in winter in India (Jena et al., 2014). The linear correlation coefficient (R^2) between OMI and AQM with the top-down emission estimates could reach 0.84 in Europe (Visser et al., 2019).

Compared to the satellite observation with relatively large uncertainty (Yang et al., 2019b; Liu et al., 2019), surface concentrations that better represent the effect of air pollution on human health and the ecosystems were less applied in the evaluation of the top-down estimates of NO_X emissions. Limited assessments were conducted at the national scale. For example, Liu et al. (2018) found that the normalized mean error (NME) between the observed and simulated NO_2 concentrations based on the top-down estimate of NO_X emissions could reach 32% in China at the resolution of 0.25°×0.25°. Besides NO_2, the estimation of NO_X emissions also play an important and complicated role on secondary air pollutant simulation including O_3 and SNA, and the response of secondary pollution to the primary emissions was commonly nonlinear. The simulated O_3 concentrations in Shanghai (the most developed city in eastern China) could increase over 20% with a 60% reduction in NO_X emissions in summer 2016, implying a clear "VOC-limit" pattern for the O_3 formation in the mega city (Wang et al., 2019). For the response of SNA to NO_X emissions, the NH_4^+ and SO_4^{2-} concentrations at an urban site in another mega city Nanjing in eastern China were simulated to increase 1.9% and 2.8% with a 40% abatement of NO_X emissions in autumn 2014, respectively, due to the weakened competition of SNA formation against SO_2 (Zhao et al., 2020). To our knowledge, however, the relatively new information from the inversed modeling of NO_X emissions has not been sufficiently incorporated into the SNA and O_3 analyses with AQM in China.

Located in eastern China, the Yangtze River Delta (YRD) region including the city of Shanghai and the provinces of Anhui, Jiangsu and Zhejiang is one of the most developed and heavy-polluted regions in the country. The air quality for most cities in YRD failed to meet National Ambient Air Quality Standard (NAAQS) Class II in 2016 (MEPPRC, 2017). NO_X emissions made great contributions to the severe air pollution in the region. Based on an offline-sampling and measurement study, for example, the annual average of the NO_3^- mass fraction to the total $PM_{2.5}$ reached 19% in Shanghai in 2014, and it was significantly elevated in the pollution event periods (Ming et al., 2017). In this study, we chose the YRD to estimate the NO_X emissions with the inversed method and to explore their influence on the air quality modeling.

The top-down estimates in NO_X emissions were firstly obtained with the nonlinear inversed method and OMI-derived NO_2 TVCDs for 2016. The advantage of the top-down estimation against on the bottom-up one was then evaluated with the AQM and abundant ground-based NO_2 concentrations. The influences of the top-down estimation in NO_X emissions were further detected on O_3 and SNA modeling. Sensitivity analyses were conducted by changing the emissions of precursors to investigate the sources and potential control approaches of O_3 and SNA pollutions for the region.

2. Data and Methods

2.1 The top-down estimation of NO_X emissions

The top-down estimation of NO_X emissions was conducted for January, April, July, and October of 2016, representing the situations of the four seasons in the YRD region, and the horizontal resolution was 9×9 km. The inversed method assumed a nonlinear and variable correlation between NO_X emissions and NO_2 TVCDs (Cooper et al., 2017), and the a posterior daily emissions (top-down estimates) were calculated with the following equations:

$$E_t = E_a\left(1+\frac{\Omega_o-\Omega_a}{\Omega_o}\beta\right) \tag{1}$$

$$\frac{\triangle E}{E} = \beta\,\frac{\triangle \Omega}{\Omega} \tag{2}$$

where E_t and E_a represent the a posterior and the a prior daily NO_X emissions, respectively; Ω_o and Ω_a represent the observed and simulated NO_2 TVCDs, respectively; β represents the response coefficient of the simulated NO_2 TVCDs to a specific change in emissions, and was calculated based on the simulated changes in TVCDs ($\Delta\Omega$) from a 10% changes in emissions (ΔE).

The inversed method assumed that the daily emissions were similar. For a given month, the a posterior daily emissions were used as the a priori emissions of the next day, and the monthly top-down estimate of the NO_X emissions was scaled from the average of the a posterior daily emissions of the last three days in the month, as the top-down estimate of daily NO_X emissions usually converged within a one-month simulation period (Zhao and Wang, 2009; Yang et al., 2019b). In our previous work (Yang et al., 2019b), we demonstrated the robustness of the method, by applying the "synthetic" TVCDs from air quality simulation based on a hypothetical "true" emission inventory, instead of those from satellite observation. We found that sufficient iteration times could result in a relatively constant emission estimate (the top-down estimate) close to the "true" emission input. From a bottom-up perspective, the difference in NO_X emissions between weekday and weekend was within 5% in the YRD region (Zhou et al., 2017), indicating an insignificant bias from the ignorance of the daily variation of emissions.

The NO_2 TVCDs were from OMI onboard the Aura satellite. It crosses the equator at 1:30 PM of local time. The horizontal resolution of OMI was 24 × 13 km at nadir (Levelt et al., 2006), one of the finest resolutions available for NO_2 TVCD observation before October 2017. We applied the Peking University Ozone Monitoring Instrument NO_2 product (POMINO v1, Lin et al., 2014; Lin et al., 2015) to constrain the NO_X emissions. POMINO v1 modified the retrieval methodology of the Dutch Ozone Monitoring Instrument NO_2 product (DOMINO v2) in China, and provided better linear correlation of NO_2 TVCDs between the satellite and available ground-based observations with the multi-axis differential optical absorption spectroscopy (MAX-DOAS) (Lin et al., 2015). The original NO_2 TVCDs from POMINO v1 (level 2) were resampled into an 18×18 km grid system based on the area weight method, and then downscaled to 9×9 km with the Kriging interpolation. As an example, the NO_2 TVCDs for July 2016 in the YRD are shown in Figure S1 in the supplement, and larger TVCDs were found in the east-central YRD.

2.2 Model configuration

The Models-3 Community Multi-scale Air Quality (CMAQ) version 5.1 was used to conduct the inversed modeling of NO_X emission estimation and to simulate the ground-level concentrations of NO_2, O_3 and SNA. As a three-dimensional Eulerian model, CMAQ includes complex interactions of atmospheric chemistry and physics and is one of the most widely applied AQM to evaluate the sources and processes of air pollution in China (UNC, 2012; Xing et al., 2015; Zheng et al., 2017). As shown in Figure 1, the two nested modeling domains were applied with their horizontal resolutions set 27 and 9 km, respectively. The mother domain (D1, 177×127 cells) included most parts of China, and the second (D2, 118 × 121 cells) covered the YRD region. The model included 28 vertical layers and the height of the first layer (ground layer) was approximately 60 m. The carbon bond gas-phase mechanism (CB05) and AERO6 aerosol module were used in the CMAQ. The initial concentrations and boundary conditions for the D1 were derived from the default clean profile, while those of D2 were extracted from the CMAQ Chemistry Transport Model (CCTM) outputs of its mother domain. The first 5 days of each simulated month were chosen as the spin-up period. Details on model configuration were described in Zhou et al. (2017) and Yang and Zhao (2019).

The Multi Resolution Emission Inventory for China (MEIC, http://www.meicmodel.org/) for 2015 was applied as the initial input of anthropogenic emissions in D1 and D2, with an original horizontal resolution at 0.1°×0.1°. In this study, the MEIC emissions from residential source were downscaled to the horizontal resolution of 9×9 km based on the spatial density of population, and those from power, industry and transportation based on the spatial distribution of gross domestic product (GDP). The NO_X emissions from soil were originally obtained from Yienger and Levy (1995) and were doubled as advised by Zhao and Wang (2009). The emissions of Cl, HCl and lightning NO_X were collected from the Global Emissions Initiative (GEIA, Price et al., 1997). Biogenic emissions were derived from the Model Emissions of Gases and Aerosols from Nature developed under the Monitoring Atmospheric Composition and Climate project (MEGAN MACC, Sindelarova et al., 2014).

Meteorological fields were provided by the Weather Research and Forecasting Model (WRF) version 3.4, a state-of-the-art atmospheric modeling system designed for both numerical weather prediction and meteorological research (Skamarock et al., 2008). The simulated parameters from WRF for D2 in January, April, July and October of 2016 were compared with the observation dataset of US National Climate

Data Center (NCDC), as summarized in Table S1 in the Supplement. The index of agreement (IOA) of wind speed for the four months between the two datasets was larger than 0.8. The Root Mean Square Error (RMSE) of wind directions for the four months was smaller than 40^o, and the index of agreement (IOA) of temperature and Relative humidity between the two datasets was larger than 0.8 and 0.7, respectively. The simulated meteorological parameters in D2 could reach the benchmarks derived from Emery et al. (2001) and Jiménez et al. (2006).

The hourly NO_2 and O_3 concentrations were observed at 230 state-operated stations of air quality monitoring in 41 cities within the YRD region, and they were applied to evaluate the model performance. Locations of the stations are indicated in Figure 1, and the observation data were derived from the China National Environmental Monitoring Center (http://www.cnemc.cn/). The observations of SO_4^{2-}, NO_3^- and NH_4^+ (SNA) concentrations in $PM_{2.5}$ for the YRD region during 2015-2017 were collected and applied to evaluate the influence of the top-down estimation of NO_X emissions on SNA simulation. In particular, the hourly SNA concentrations of $PM_{2.5}$ at Jiangsu Provincial Academy of Environmental Science, an urban site in the capital city of Jiangsu Province, Nanjing (JSPAES; Chen et al., 2019b), were observed with the Monitor for Aerosols and Gases in ambient Air (MARGA; Metrohm, Switzerland) for January, April, July and October 2016. Meanwhile, the daily average concentrations of SNA were also available from MARGA measurement for the four months at the Station for Observing Regional Processes and the Earth System, a suburban site in eastern Nanjing (SORPES; Ding et al., 2019). Besides, the seasonal average concentrations of SNA were available at another four sites in YRD, including the Nanjing University of Information Science & Technology site in Nanjing (NUIST, Zhang, 2017), and three sites respectively in the cities of Hangzhou (HZS; Li, 2018), Changzhou (CZS; Liu et al., 2018) and Suzhou (SZS; Wang et al., 2016). Details of the collected SNA measurement studies are summarized in Table S2 in the supplement, and the locations of those sites are illustrated in Figure 1.

2.3 Scenario setting of sensitivity analysis

In general, there are two categories of chemical regimes (VOC-limited and NOx-limited) in O_3 formation (Wang et al., 2009; Jin et al., 2017). In the VOC-limited regime, growth in O_3 concentrations occurs with increased VOCs emissions and declined NO_X emissions, while the increased NO_X emissions result in enhancement of O_3 concentrations in the NOx-limited regime. To explore the sources and potential control approaches of O_3 pollution, the sensitivity of O_3 formation to its precursor emissions for April was analyzed with CMAQ modeling in the YRD region. In YRD, the peaking time of O_3 concentration has gradually moved from summer to late spring, and the mean observed O_3 concentration in April was 72.5 $\mu g/m^3$, slightly higher than that in July (71.9 $\mu g/m^3$). In addition, the model performance of O_3 was better for April than that for July in this work (see details in Section 3.2). Therefore, we selected April to explore the sensitivity analysis of O_3 formation in the region. As summarized in Table S3 in the supplement, eight cases were set besides the base scenario with the top-down NO_X estimates for April 2016. Cases 1 and 6 reduced only the NO_X emissions by 30% and 60%, and Cases 2 and 7 reduced only the VOC_S emissions by 30% and 60%, respectively. To explore the co-effect of VOCs and NO_X emission controls on O_3 concentrations, cases with different reduction rates of VOCs and NO_X emissions were designed. The emissions of NO_X and VOCs in Case 4 were decreased by 30% and 60%, and in Case 5 by 60% and 30%, respectively. Both NO_X and VOCs emissions were reduced 30% and 60% in Cases 3 and 8, respectively.

The response of SNA concentrations to the changes in precursor emissions was influenced by various factors including the abundance of NH_3, atmospheric oxidation, and the chemical regime of O_3 formation (Wang et al., 2013; Cheng et al., 2016; Zhao et al., 2020). To explore the sensitivity of SNA formation to its precursor emissions, four cases were set besides the base scenario for January 2016, the month with the largest observed SNA concentrations. As shown in Table S4 in the supplement, the emissions of NO_X, SO_2 and NH_3 were reduced by 30% in Cases 9-11, respectively, and the emissions of NO_X, SO_2 and NH_3 were simultaneously decreased by 30% in Case 12.

3. Results and discussion

3.1 Evaluation of the bottom-up and top-down estimates of NO_X emissions

Figure 2 compares the magnitude of the NO_X emissions estimated based on the bottom-up (MEIC) and top-down methods by month in the YRD region. The top-down estimates were smaller than the bottom-up ones for all the concerned four months, and the average of the monthly NO_X emissions were calculated at 260.0 Gg/month for 2016 with the top-down method, 24% smaller than the bottom-up estimation. The comparison indicates a probable overestimation in NO_X emissions with current bottom-up methodology, attributed partly to the insufficient consideration of the effect of recent control on emission abatement. Stringent measures have gradually been conducted to improve the local air quality in the YRD region. For example, the “ultra-low” emission policy for power sector started in 2015, requiring the NO_X concentration in the flue gas of coal-fired unit the same as that of gas-fired unit. The technology retrofitting on power units have been widely conducted, significant improving the NO_X removal efficiencies of selective catalytic reduction (SCR) systems. Those detailed changes in emission control, however, could not be fully and timely incorporated into the national emission inventory that relied more on the routinely reported information and policy of environmental management over the country. With the on-line data from continuous emission monitoring systems (CEMS) incorporated, the NO_X emissions from power sector were estimated to be 53% smaller than MEIC for the China in 2015 in our previous work (Zhang et al., 2019). The bias between the top-down and bottom-up estimates could be larger in earlier years and reduced more recently. According to Yang et al. (2019b) and Qu et al. (2017), for example, the top-down NO_X emissions were 44% and 31% smaller than bottom-up ones for the YRD region and the whole China in 2012. Benefiting from the better data availability, the bottom-up inventory has been improved with the inclusion of more information on individual power and industrial plants for recent years (Zheng et al., 2018).

The differences in the spatial distribution of NO_X emissions between the bottom-up and top-down estimates are illustrated by month for the YRD in Figure 3. The top-down estimates were commonly smaller than the bottom-up ones in the east-central YRD with intensive manufacturing industry and population, and larger than those in most of Zhejiang Province with more hilly and suburban regions. The bias might result from following issues. From a bottom-up perspective, on one hand, more stringent control measures were preferentially conducted for power and industrial plants in regions with heavier air pollution like east-central YRD. As mentioned above, the effects of such actions were difficult to be fully tracked in the bottom-up inventory, leading to the overestimation in emissions for those regions. Due to the lack of precise locations of individual industrial plants (except for large point sources), moreover, the spatial allocation of the emissions relied commonly on the densities of population and economy, assuming a strong correlation with emissions for them. Such assumption, however, would not still hold in recent years, as a number of factories in the relatively developed region were moved to the less developed suburban regions (e.g., southern Zhejiang) for both environmental and economic purposes. The insufficient consideration of the movings of emission sources was thus expected to result in overestimation in emissions for developed regions and underestimation for the less developed. On the other hand, the satellite-derived TVCDs were relatively small in southern Zhejiang (Fig. S1), and larger error in satellite retrieval and thereby emission constraining with the inversed modeling was expected.

Figure 4 illustrates the observed and simulated hourly NO_2 concentrations using the bottom-up and top-down estimates of NO_X emissions in the CMAQ by month. The NO_2 concentrations simulated with the bottom-up estimates were clearly larger than the observation in all the four concerned months, with the largest and smallest normalized mean bias (NMB) reaching 111% and 34 % for July and January, respectively. The result suggests again the overestimation in NO_X emissions in the current bottom-up inventory for the YRD. The model performance based on the top-down estimates was much better than that based on the bottom-up ones, indicating that the inversed modeling with satellite observation constraint effectively improved the estimation of NO_X emissions. The biggest improvement was found for July, with the NMB reduced from 111% to -0.4% and the NME reduced from 111% to 33%. As shown in Fig. 2, relatively big reduction from the bottom-up to top-down estimation in NO_X emissions was found for July compared to most of other months.

Scatter plots of the annual means of the observed and simulated surface NO_2 concentrations are shown in Figure S2 in the supplement. The slope between the observation and simulation with the top-down estimate (0.99) was much closer to 1 than that with the bottom-up one (1.57), indicating clearly the advantage of the top-down method on the constraining of the magnitude of the total emissions in the YRD region. The difference in the two slopes implies that the surface NO_2 concentrations simulated with the bottom-up estimation were over 50% larger than those based on top-down ones. As a comparison, the total emissions in the bottom-up inventory were only 30% larger than the top-down estimation for the whole YRD region. The larger overestimation in the concentrations than the emissions from the bottom-up inventory could result partly from the bias of the locations of state-operated ground observation sites. Most of those sites were located in the urban areas where excess emissions were allocated according to the high density of economy and population, and elevated concentrations were thus simulated compared to rural areas. The similar correlation coefficients (R) suggested that the spatial distribution of NO_X emissions was not greatly improved in the top-down estimation on an annual basis of urban observation. Uncertainty existed in the satellite observation: the NMB between NO_2 TVCDs in POMINO and available ground-based MAX-DOAS observations was 21% in cloud-free days (Liu et al., 2019). Due mainly to the NO_X transport, moreover, a bias of 13%-33% on the spatial distribution of emissions was estimated for the inversed method at the horizontal resolution of 9 km or finer (Yang et al., 2019b). Inclusion of more available observation in rural areas helps improve the comprehensive evaluation of emission estimation.

Figure 5 illustrates the spatial distribution of monthly mean NO_2 concentrations simulated based on the top-down estimates and the differences between the simulations with the top-down and bottom-up ones. The larger NO_2 concentrations existed in the east-central YRD for all the months (left column in Fig. 5), and the difference in spatial distribution of NO_2 concentrations (right column in Fig. 5) was similar with that in NO_X emissions (Fig. 3). Larger reduction in NO_2 concentrations based on the top-down estimates was commonly found in east-central YRD, while the increased concentrations were found in most of Zhejiang.

3.2 Evaluation of the O_3 simulation based on the top-down NO_X estimates

Figure 6 shows the observed and simulated hourly O_3 concentrations based on the bottom-up and top-down estimates of NO_X emissions by month. Indicated by the smaller NMBs and NMEs, the model performance of O_3 based on the top-down estimates was better than that based on the bottom-up ones for most months. It suggests that the constrained NO_X emissions with satellite observation could play an important role on the improvement of O_3 simulation. The largest improvement was found in January, for which the NMB and NME were changed from -44% and 49% to 13% and 40%, respectively, attributed to the biggest change in NO_X emissions between the top-down and bottom-up estimates for the month. The worse O_3 modeling performance was found for July when the top-down estimate instead of the bottom-up one was applied in the simulation, indicated by the increased NMB and NME. Since the top-down estimation of NO_X emissions was justified by the improved NO_2 simulation in July (Fig. 4c), the worse O_3 simulation might result from the uncertainty in emissions of the volatile organic compounds (VOCs) and the chemical mechanism of AQM in summer. As suggested by Li (2019), the biogenic VOCs (BVOCs) emissions of the YRD region could be overestimated by 121% in summer attributed to ignoring the effect of droughts, and such overestimation might elevate the O_3 concentrations in AQM. In order to explore the influence of uncertainty of BVOCs emissions on O_3 model performance, we conducted an extra case in which the BVOCs emissions were cut by 50% in CMAQ. As shown in Figure S3 in the supplement, the NMB between the observed and simulated O_3 based on the top-down estimate of NO_X emissions and the reduced BVOCs emissions declined 27% in July. However, it was still larger than the NMB at 1.1% when the bottom-up estimate of

NO_X emissions was applied (Fig. 4c). This comparison thus suggested that the complicated mechanism for summer O_3 formation was insufficiently considered in current model. A recent study conducted an intercomparison of surface-level O_3 simulation from 14 state-of-the-art chemical transport models, and implied that the larger overestimation of summer O_3 than winter for eastern China resulted possibly from the uncertainty in the photochemical treatment in models (Li et al., 2019).

Table 1 summarizes the observed and simulated daily maximum 8-hour averaged (MDA8) O_3 concentrations based on the bottom-up and top-down estimates of NO_X emissions are summarized by month for the YRD region. The MDA8 O_3 concentrations simulated with the top-down estimates were larger than those with the bottom-up ones, and were closer to the observation for most months. As most of the YRD was identified as the VOC-limited region (Li et al., 2012; Zhou et al., 2017), the reduced NO_X emissions with the top-down method enhanced the O_3 levels in the AQM. Similar to the hourly concentrations, the most significant improvement for MDA8 was found in January, with the NMB and NME reduced from -35% and 39% to 11% and 28%, respectively. Moreover, the improvement of April and October for MDA8 was larger than that for the hourly concentrations, indicating that the improved NO_X emissions were more beneficial for the simulation of daytime peak O_3 concentrations in spring and winter. Figure 7 illustrates the spatial distribution of the monthly mean O_3 concentrations simulated based on the top-down NO_X estimates and the differences between the simulations with the top-down and bottom-up estimates by month. In contrast to NO_2, the smaller O_3 concentrations existed in the east-central YRD for most months, as it was identified as the VOC-limited region with relatively high NO_2 level (Wang et al., 2019). Larger O_3 concentrations were found for the surrounding regions in the YRD, e.g., southern Zhejiang, attributed partly to the relatively abundant BVOC emissions (Li, 2019). An exception existed for July, with clearly larger O_3 concentrations in east-central YRD. With the largest population density and most developed economy in YRD, the area contains a large number of chemical industrial plants and solvent storage, transportation and usage (Zhao et al., 2017). High temperature in summer promoted the volatilization of chemical products and solvent, and thereby enhanced the seasonal VOCs emissions more significantly compared to other less developed YRD regions. Moreover, the lowest NO_2 concentration found in summer helped increase the O_3 concentration for the region (Gu et al., 2020). Regarding the simulation difference with two emission estimates, application of the top-down estimates instead of the bottom-up ones elevated the O_3 concentrations in most of the YRD region. In particular, the big reduction in NO_X emissions for the east-central YRD (Fig. 3) was expected to be responsible for the evident growth in O_3 concentrations. As east-central YRD was identified as a VOC-limited region in terms of O_3 formation, the O_3 concentration in the region would be elevated along with the reduced NO_X emissions, reflecting the negative effect of NO_X control on O_3 pollution alleviation (Wang et al., 2019).

3.3 Evaluation of SNA simulation based on the top-down NO_X estimates

Shown in Table 2 is the comparison between the observed and simulated SNA (SO_4^{2-}, NO_3^- and NH_4^+) concentrations by season. Larger observed and simulated SNA concentrations were found in winter and spring, and smaller were found in summer and autumn. For most seasons, the simulations of NO_3^- concentrations were moderately improved with the top-down estimates of NO_X emissions for all the concerned YRD cities, with an exception of Nanjing in autumn. The largest improvement was found in summer, with the mean bias between the simulation and observation reduced 35% for all the involved cites. Compared to the bottom-up inventory, the commonly smaller NO_X emissions in the top-down estimates limited the NO_2 concentration and suppressed the formation of NO_3^-, while the enhanced O_3 from the reduced NO_X emissions promoted it (Cai et al., 2017; Huang et al., 2020). In summer, the former dominated the process with the most evident improvement in NO_2 simulation (Figure 4), thus the reduced NO_3^- concentrations that were closer to observation were simulated for all the cities.

The simulations with both top-down and bottom-up estimates of NO_X emissions underestimated the NH_4^+ concentrations for most cases, and such underestimation was slightly corrected with the application of the top-down estimates except for summer.

The average change in NH_4^+ concentrations was 2.3%, much smaller than that of NO_3^- at 14%. The moderate improvement in NH_4^+ simulation with the reduced NO_X emissions in the top-down estimates resulted partly from the enhancement of the simulated O_3 concentrations and thereby the promoted NH_4^+ formation. In summer, however, the significant drop in the simulated NO_2 concentration was assumed to reduce the NO_3^- and NH_4^+ formation, and to weaken the consistency between the simulated and observed NH_4^+. The difference between the simulated SO_4^{2-} with the bottom-up and top-down NO_X emission estimates were small for most seasons, implying a limited benefit of improved NO_X emissions on SO_4^{2-} modeling. Besides emission data, the chemical mechanisms included in the model should be important for the model performance. For example, adding SO_2 heterogeneous oxidation in the model could largely improve the sulfate simulation in Nanjing (Sha et al., 2019)

Figure 8 shows the differences in the spatial distribution of SNA concentrations simulated with the bottom-up and top-down estimates of NO_X emissions by month. In most of the region, the differences of NO_3^- concentrations were larger than those of NH_4^+ and SO_4^{2-} for all seasons, and they were mainly controlled by the changed ambient NO_2 or O_3 level. The difference in spatial pattern of NO_3^- was similar to that of O_3 for January, and the larger growth attributed to the application of the top-down estimates was found in northern Anhui and eastern Zhejiang (Fig. 8a). The result implies that the change in NO_3^- concentration in winter could result partly from the improved O_3 simulation, i.e., the elevated O_3 was an important reason for the enhanced the formation of SNA in winter (Huang et al., 2020). Similarly, the increased NO_3^- was found for more than half of the YRD region in April, along with the growth of O_3 concentrations (Fig. 8d). For July, however, the difference in spatial pattern of NO_3^- (Fig. 8g) was similar with NO_2 (Fig. 5g), and the larger reduction attributed to the application of the top-down estimates was found in northern YRD. The result suggests that the declining NO_X emissions and thereby NO_2 concentration dominated the reduced NO_3^- formation in summer. It was mainly because the reduction of top-down NO_X emission estimate from the bottom-up emission inventory was much larger for July compared to spring or autumn (Fig 2). In addition, the

VOC-limit mechanism in O_3 formation was found weaker in summer than winter (see Fig. 7e and Fig. 7g), resulting in less O_3 formation and thereby nitrate aerosol through oxidation. In October, the growth in NO_3^- concentrations was found again in most YRD when the top-down estimates were applied (Fig. 8j). The growth in the north resulted mainly from the increased O_3 level, while that in the south was associated with the increased NO_2. The differences in spatial patterns of simulated NH_4^+ concentrations were similar to those of NO_3^- for the four months, suggesting that the change in NH_4^+ was associated with formation and decomposition of NH_4NO_3. However, the changes of spatial distribution of SO_4^{2-} were similar with those of O_3 concentration. Since NH_4^+ was preferred to react with SO_4^{2-} rather than NO_3^- (Wang et al., 2013), the formation of SO_4^{2-} was mainly influenced by the atmospheric oxidizing capacity when only NO_X emissions were changed.

Figure 9 illustrates the observed and simulated hourly NO_3^- concentrations based on the bottom-up and top-down estimate of NO_X emissions by month at JSPAES. The NMBs and NMEs for simulation with the top-down emissions were smaller than those with bottom-up ones in January and July, implying the benefit of the improved NO_X emissions on hourly NO_3^- concentration simulation in winter and summer. The best model performance with the top-down estimates was found in January, with the hourly variation commonly caught with AQM. However, the NO_3^- concentration was seriously overestimated and the model failed to catch the hourly variations in summer indicated by the large NMB and NME. As shown in Figure S4 in the supplement, both the NO_2 and O_3 concentrations at JSPAES were significantly overestimated for July except O_3 with the bottom-up NO_X emission estimate, and it partly explained the elevated NO_3^- level from CMAQ simulation.

Figures S5 and S6 in the supplement compare the observed and simulated hourly concentrations at JSPAES by month for NH_4^+ and SO_4^{2-}, respectively. The NMBs and NMEs for NH_4^+ simulation with the top-down estimates were smaller than those with the bottom-up ones for most months, while the changes in SO_4^{2-} concentration were small. The NH_4^+ and SO_4^{2-} concentrations were largely underestimated with the top-down estimates in January, indicated by the NMB at -44% and -38%, respectively.

Meanwhile, as shown in Figure S7 in the supplement, the SO_2 concentrations were overestimated by 61% at the site. The results thus imply a great uncertainty in the gas-particle partitioning of $(NH_4)_2SO_4$ formation in the model in winter, attributed probably to the missed oxidation mechanisms of SO_2 (Chen et al., 2019c).

3.4 Sensitivity analysis of O_3 and SNA formation in the YRD region

Table 3 summarizes the relative changes in the simulated O_3 concentrations for April 2016 in different cases. The mean O_3 concentration would decline by 8.9% and 19.5% with 30% and 60% VOCs emissions off (Cases 2 and 7), while it would increase by 14.2% and 23.7% with 30% and 60% NO_X emissions off (Cases 1 and 6), respectively. The result confirmed the VOC-limited regime of O_3 formation in the YRD region: controlling VOCs emissions was an effective way to alleviate O_3 pollution, while reducing NO_X emissions alone would aggravate O_3 pollution.

The growth of O_3 concentrations was also found when the reduction rate of NO_X emissions was equal to or larger than that of VOCs. The O_3 concentration would increase by 7.1% and 14.5% respectively when both NO_X and VOCs emissions were reduced by 30% and 60% (Cases 3 and 8), and it would increase by 19.8% when NO_X and VOCs emissions were respectively declined by 60% and 30% (Case 5). In contrast, small abatement of O_3 concentrations (2.1%) was achieved from the 30% and 60% reduction of emissions respectively for NO_X and VOCs (Case 4), implying that the O_3 level could be restrained when the reduction rate of VOCs was twice of or more than that of NO_X. To control the O_3 pollution effectively and efficiently, therefore, the magnitude of VOCs and NO_X emission reduction should be carefully planned and implemented. In actual fact, controlling VOCs is more difficulty than NO_X. Compared to NO_X that comes mainly from fossil fuel combustion (Zheng et al., 2018), it is more complicated to identify the sources of specific VOCs species that are most active in O_3 formation (Wei et al., 2014; Zhao et al., 2017). Moreover, substantial VOC emissions are from area or fugitive sources, for which the emission control technology can hardly be effectively applied. Therefore, it is a big challenge to control O_3 pollution by reducing more VOCs than NO_X.

Figure 10 illustrates the differences in spatial patterns of the simulated monthly mean O_3 concentrations between the base and sensitivity cases in April. The O_3 concentrations were expected to decline for the whole YRD region in the cases of 30% and 60% VOCs emissions off (Fig. 10b and 10d), indicating the VOC-limited regime of O_3 formation for the entire YRD. For other cases, the O_3 concentrations were clearly elevated in the central-eastern YRD with relatively large population and developed industry, particularly for the cases with NO_X control only (Fig. 10a and 10c) or relatively large NO_X abatement together with VOC control (Fig. 10f and 10g). Even for the case with 60% of VOCs reduction and 30% of NO_X (Fig. 10h), there was still small increase in O_3 concentration in central-eastern YRD, in contrast to the slight O_3 reduction found for most of YRD areas. Those results reveal the extreme difficulty in O_3 pollution control for the region. In southwestern Zhejiang, the O_3 concentrations were found to decline in the cases with large abatement of NO_X emissions (Fig. 10c, 10f and 10g), suggesting a shifting from VOC-limited to NO_X limited region for the O_3 formation.

Table 4 summarizes the change in the simulated monthly means of SNA (NO_3^-, NH_4^+ and SO_4^{2-}) concentrations between the base case and sensitivity cases in January. The SNA concentrations were decreased in most cases, implying that the reduction in precursor emissions was useful for mitigating the SNA pollution. Compared to that of precursor emissions, however, the reduction rate of SNA was much smaller attributed to the strong nonlinearity of SNA formation. The largest reductions were found at 11.7% and 12.4% when emissions of NH_3 and all the three precursors were decreased by 30% (Cases 11 and 12), respectively. In contrast, the SNA concentrations declined slightly by 1% and increased by 0.5% when NO_X and SO_2 emissions were reduced by 30% (Cases 9 and 10), respectively. The results suggest that most of YRD was in an NH_3-neutral or even NH_3-poor condition in winter, consistent with the judgment through AQM based on an updated NH_3 emission inventory (Zhao et al., 2020), as the NH_3 volatilization in winter was much smaller than other seasons. Reducing NH_3 emissions was the most efficient way to control SNA pollution for the region in winter. In Case 11 with NH_3 control only, the reduced NO_3^- and NH_4^+ were much larger than that of SO_4^{2-}. As NH_3 reacted with SO_2 prior to NO_X, NH_4NO_3 was assumed easier to decompose than $(NH_4)_2SO_4$ when NH_3 emissions were reduced. The growth of NO_3^- concentrations was found for Case 10 (SO_2 control only), since the free NH_3 from the reduced SO_2 emissions could react with NO_X in the NH_3-poor condition. Similarly, the SO_4^{2-} concentrations increased for Case 9 (NO_X control only), as the elevated O_3 attributed to the reduction of NO_X emissions promoted the SO_4^{2-} formation.

4. Summary

From a "top-down" perspective, we have estimated the monthly NO_X emissions for the YRD region in 2016, based on the nonlinear inversed modeling and NO_2 TVCDs from POMINO, and the bottom-up and top-down estimates of NO_X emissions were evaluated with AQM and ground NO_2 observation. Due to insufficient consideration of improved controls on power and industrial sources, the NO_X emissions were probably overestimated in current bottom-up inventory (MEIC), resulting in significantly higher simulated NO_2 concentrations than the observation. The simulated NO_2 concentrations with the top-down estimates were closer to the observation for all the four seasons, suggesting the improved emission estimation with satellite constraint. Improved O_3 and SNA simulations with the top-down NO_X estimates for most months indicate the importance role of precursor emission estimation on secondary pollution modeling for the region. Through the sensitivity analysis of O_3 formation, the mean O_3 concentrations were found to decrease for most YRD when only VOCs emissions were reduced or the reduced rate of VOCs was twice of NO_X, and the result indicates the effectiveness of controlling VOCs emissions on O_3 pollution abatement for the region. For part of southern Zhejiang, however, the O_3 concentrations were simulated to decline with the reduced NO_X emissions, implying the shifting from VOC-limited to NO_X-limited region. Compared to reducing NO_X or SO_2 only, larger reduction in SNA concentrations was found when 30% of emissions were cut for NH_3 or all the three precursors (NO_2, NH_3 and SO_2). The result suggests that reducing NH_3 emissions was crucial to alleviate SNA pollution of YRD in winter.

Limitations remain in this study. Due to the limited horizontal resolution of OMI, relatively big bias existed in the spatial distribution of the constrained NO_X emissions at the regional scale compared to national or continental one, and the uncertainty could exceed 30% for the YRD region (Yang et al., 2019b). Therefore the improvement on the top-down estimates of NO_X emissions can be expected when the more advanced and reliable products of satellite observation get available at finer horizontal resolution (e.g., TROPOspheric Monitoring Instrument, TROPOMI). Besides, more SNA observations from on-line measurement are recommended for a better space coverage and temporal resolution, to explore more carefully the response of SNA to the changes in emissions of NO_X and other precursors.

Data availability

All data in this study are available from the authors upon request.

Author contributions

YY developed the strategy and methodology of the work and wrote the draft. YZ improved the methodology and revised the manuscript. LZ provided useful comments on the methodology. JZ and XH provided observation data of secondary inorganic aerosols. XZ, YZ, MX and YL provided comments on air quality modeling.

Competing interests

The authors declare that they have no conflict of interest.

Acknowledgements

This work was sponsored by Natural Science Foundation of China (91644220 and 41575142), the National Key Research and Development Program of China (2017YFC0210106), and the Key Program for Coordinated Control of $PM_{2.5}$ and

Ozone for Jiangsu Province (2019023). We would also like to thank Tsinghua University for the free use of national emissions data (MEIC), and Peking University for the support of satellite data (POMINO v1).

References

Cai, S., Wang, Y., Zhao, B., Chang, X., Hao, J. M.: The impact of the “Air Pollution Prevention and Control Action Plan” on $PM_{2.5}$ concentrations in Jing-Jin-Ji region during 2012-2020, Sci. Total Environ., 580, 197-209, 2017.

Chen, D., Tian, X., Lang J., Zhou, Y., Li, Y., Guo, X. Wang, W., Liu, B.: The impact of ship emissions on $PM_{2.5}$ and the deposition of nitrogen and sulfur in Yangtze River Delta, China, Sci. Total Environ., 649, 1609-1619, 2019a.

Chen, D., Zhao, Y., Lyu, R., Wu, R., Dai, L., Zhao, Y., Chen, F., Zhang, J., Yu, H., Guan, M.: Seasonal and spatial variations of optical properties of light absorbing carbon and its influencing factors in a typical polluted city in Yangtze River Delta, China. Atmos. Environ., 199, 45-54, 2019b.

Chen, L., Gao, Y., Zhang, M., Fu, J. S., Kurokawa, J. I.: Mics-Asia III: multi-model comparison and evaluation of aerosol over East Asia, Atmos. Chem. Phys., 19, 11911-11937, 2019c.

Cheng, Y. F., Zheng, G. J., Wei, C., Mu, Q., Zheng, B., Wang, Z. B., Gao, M., Zhang, Q., He, K. B., Carmichael, G., Pöschl, U., Su H.: Reactive nitrogen chemistry in aerosol water as a source of sulfate during haze events in China, Sci. Adv., 2(e1601530), 1-11, 2016.

Cooper, M., Martin, R.V., Padmanabhan, A., Henze, D.K.: Comparing mass balance and adjoint methods for inverse modeling of nitrogen dioxide columns for global nitrogen oxide emissions, J. Geophys. Res.: Atmosphere, 122, 4718–4734, 2017.

de Foy, B., Lu, Z., Streets, D.G., Lamsal, L.N., Duncan., B.N.: Estimates of power plant NOx emissions and lifetimes from OMI NO_2 satellite retrievals, Atmos. Environ., 116, 1-11, 2015.

Ding, A., Huang, X., Nie, W., Chi, X., Xu, Z., Zheng, L., Xu, Z., Xie, Y., Qi, X., Shen, Y., Sun, P., Wang, J., Wang, L., Sun, J., Yang, X., Qin, W., Zhang, X., Cheng, W., Liu, W., Pan, L., Fu, C.: Significant reduction of $PM_{2.5}$ in eastern China due to regional-scale emission control: evidence from SORPES in 2011–2018, Atmos. Chem. Phys., 19, 11791–11801, 2019.

Emery, C., Tai, E., Yarwood, G.: Enhanced meteorological modeling and performance evaluation for two Texas episodes, Report to the Texas Natural Resources Conservation Commission, prepared by ENVIRON, International Corp, Novato, CA , 2001.

Granier, C., Bessagnet, B., Bond, T., Angiola A.D., van der G.H.D. , Frost G.J. , Heil A., Kaiser J.W., Kinne S., Klimont Z., Kloster S., Lamarque J.F., Liousse C., Masui T., Meleux, F., Mieville, A., Ohara, T., Raut, J.C., Riahi, K., Schultz, M.G., Smith, S.J., Thompson, A., van Aardenne, J., van der Werf, G.R., van Vuuren, D.P.: Evolution of anthropogenic and biomass burning emissions of air pollutants at global and regional scales during the 1980–2010 period. Climatic Change, 109, 163-190, 2011.

Gu, D.S., Wang, Y.X., Smeltzer, C., Boersma, K.F.: Anthropogenic emissions of NOx over China: Reconciling the difference of inverse modeling results using GOME-2 and OMI measurements, J. Geophys. Res.: Atmosphere, 119, 7732-7740, 2014.

Gu, Y. X., Li, K., Xu, J. M., Liao, H., Zhou, G. Q.: Observed dependence of surface ozone on increasing temperature in Shanghai, China, Atmos. Environ., 221, 1–10, 2020.

Huang, X., Ding, A. J., Gao, J., Zheng, B., Zhou, D. R., Qi, X. M., Tang, R., Ren, C. H., Nie, W., Chi, X. G., Wang, J. P., Xu, Z., Chen, L. D., Li, Y. Y., Che, F., Pang, N. N., Wang, H. K., Tong, D., Qin, W., Cheng, W., Liu, W. J., Fu, Q. Y., Chai, F. H., Davis, S. J., Zhang, Q., He K. B.: Enhanced secondary pollution offset reduction of primary emissions during COVID-19 lockdown in China, Natl. Sci. Rev., nwaa137, https://doi.org/10.1093/nsr/nwaa137, 2020.

Jena, C., Ghude, S. D, Beig, G., Chate, D. M., Kumar, R, Pfister, G. G., Lal, D. M., Surendran, D. E., Fadnavis, S., van der A, R. J.: Inter-comparison of different NO_X emission inventories and associated variation in simulated surface ozone in Indian region, Atmos. Environ., 17, 61-73, 2014.

Jiménez, P., Jorba, O., Parra R., Baldasano, J. M.: Evaluation of MM5-EMICAT2000-CMAQ performance and sensitivity in complex terrain: High-resolution application to the northeastern Iberian Peninsula, Atmos. Environ., 40, 5056-5072, 2006.

Jin, X. M., Fiore, A. M., Murray, L. T., Valin, L. C., Lamsal, L. N., Duncan, B., Boersma, K. F., De Smedt, I., Abad ,G. G., Chance, K., Tonnesen, G. S.: Evaluating a space-based Indicator of surface ozone-NOx-VOC sensitivity over midlatitude source regions and application to decadal trends, J. Geophys. Res.-Atmos., 122, 10231–10253, 2017.

Kong, H., Lin J.T., Zhang, R.X., Liu, M.Y., Weng, H.J., Ni, R.J., Chen, L.L., Wang, J.X., Zhang, Q.: High-resolution (0.05° × 0.05°) NOx emissions in the Yangtze River Delta inferred from OMI, Atmos. Chem. Phys., 19, 12835-12856, 2019.

Kurokawa, J.I., Yumimoto, K., Uno, I., Ohara, T.: Adjoint inverse modeling of NOx emissions over eastern China using satellite observations of NO_2 vertical column densities, Atmos. Environ., 43, 1878-1887, 2009.

Levelt, P.F., Hilsenrath, E., Leppelmeier, G.W., van den Oord, G.H.J., Bhartia, P.K., Tamminen, J., de Haan, J.F., Veefkind, J.P.: Science objectives of the Ozone Monitoring Instrument, IEEE T. Geosci. Remote, 44, 1199-1208, 2006.

Li, L.: The numerical simulation of comprehensive air pollution characteristics in a typical city-cluster, Doctoral dissertation, Shanghai University, Shanghai, China, 2012.

Li, L.: Application of new generation natural source emission model in Yangtze River Delta and its influence on SOA and O_3 (in Chinese), The 4th application technology seminar on air pollution source emission inventory in China, Nanjing, China, September 18-19, 2019.

Li, J., Nagashima, T., Kong, L., Ge, B., Yamaji, K., Fu, J.S., Wang, X., Fan, Q., Itahashi, S., Lee, H.J., Kim, C.H., Lin, C.Y., Zhang, M., Tao, Z., Kajino, M., Liao, H., Li, M., Woo, J.H., Kurokawa, J., Wang, Z., Wu, Q., Akimoto, H., Carmichae, G. R., and Wang, Z.: Model evaluation and intercomparison of surface-level ozone and relevant species in East Asia in the context of MICS-Asia Phase III – Part 1: Overview, Atmos. Chem. Phys., 19, 12993-13015, 2019.

Li, Z.: Seasonal pollution characteristics and cytotoxicity of $PM_{2.5}$ in district of Hangzhou City (in Chinese), Master thesis, Zhejiang University, Hangzhou, China, 2018.

Lin, J. T., Martin, R. V., Boersma, K. F., Sneep, M., Stammes, P., Spurr, R., Wang, P., Van Roozendael, M., Clémer, K., Irie, H.: Retrieving tropospheric nitrogen dioxide from the Ozone Monitoring Instrument: Effects of aerosols, surface reflectance anisotropy, and vertical profile of nitrogen dioxide, Atmos. Chem. Phys., 14, 1441-1461, 2014.

Lin, J. T., Liu, M. Y., Xin, J. Y., Boersma, K. F., Spurr, R., Martin, R., Zhang, Q.: Influence of aerosols and surface reflectance on satellite NO_2 retrieval: seasonal and spatial characteristics and implications for NOx emission constraints, Atmos. Chem. Phys., 15, 11217-11241, 2015.

Liu, F., van der, A R., Eskes, H., Ding, J., Mijling, B.: Evaluation of modeling NO_2 concentrations driven by satellite-derived and bottom-up emission inventories using in situ measurements over China, Atmos. Chem. Phys., 18, 4171-4186, 2018.

Liu, J. S.，Gu, Y.，Ma, S. S.，Su, Y. L.，Ye, Z. L.: Day-night differences and source apportionment of inorganic components of $PM_{2.5}$ during summer-winter in Changzhou city (in Chinese), Environ. Sci., 39, 980-989, 2018.

Liu, M.Y., Lin, J.T., Boersma, K.F., Pinardi, G., Wang, Y., Chimot, J., Wagner, T., Xie, P., Eskes, H., Van Roozendael, M., Hendrick, F., Wang, P., Wang, T., Yan, Y.Y., Chen, L.L., Ni, R.J.: Improved aerosol correction for OMI tropospheric NO_2 retrieval over East Asia: constraint from CALIOP aerosol vertical profile, Atmos. Measure. Tec., 12, 1-21, 2019.

Martin, R.V., Jacob, D.J., Chance, K., Kurosu, T.P., Palmer, P.I., Evans, M.J.: Global inventory of nitrogen oxide emissions constrained by space-based observations of NO_2 columns, J. Geophys. Res., 108, 1-12, 2003.

Ming, L. L., Jin, L., Li J., Yang, W. Y., Liu, D., Zhang, G., Wang, Z. F., Lia, X. D.: $PM_{2.5}$ in the Yangtze River Delta, China: Chemical compositions, seasonal variations, and regional pollution events, Environ. Pollut., 223, 200-212, 2017.

Ministry of Environmental protection of the People’s Republic of China (MEPPRC): Chinese Environmental Situation Communique in 2016, Beijing, 2017.

Miyazaki, K., Eskes, H. J., and Sudo, K.: Global NOx emission estimates derived from an assimilation of OMI tropospheric NO_2 columns, Atmos. Chem. Phys., 12, 2263–2288, 2012.

Price, C., Penner, J., Prather, M.: NO_X from lightning, Part I: Global distribution based on lightning physics, J. Geophys. Res.: Atmospheres, 102, D5, 1-5, 1997.

Qu, Z., Henze, D.K., Capps, S.L., Wang, Y., Xu, X., Wang, J., Keller, M., Monthly top-down NOx emissions for China (2005–2012): A hybrid inversion method and trend analysis, J. Geophys. Res.: Atmosphere, 122, 4600-4625, 2017.

Saikawa, E., Kim, H., Zhong, M., Zhao, Y., Janssens-Maenhout, G., Kurokawa, J., Klimont, Z., Wagner, F., Naik, V., Horowitz, L.W., Zhang, Q.: Comparison of emissions inventories of anthropogenic air pollutants and greenhouse gases in China, Atmos. Chem. Phys., 17, 6393-6421, 2017.

Sha, T., Ma, X., Jia, H., Tian, R., Chang, Y., Cao, F., Zhang, Y.: Aerosol chemical component: Simulations with WRF-Chem and comparison with observations in Nanjing, Atmos. Environ., 218(116982), 1-14, 2019.

Sindelarova, K., Granier, C., Bouarar, I., Guenther, A., Tilmes, S., Stavrakou, T., Müller, J.F., Kuhn, U., Stefani, P., Knorr, W.: Global data set of biogenic VOC emissions calculated by the MEGAN model over the last 30 years, Atmos. Chem. Phys., 14, 9317–9341, 2014.

Skamarock, W. C., Klemp, J. B., Dudhia, J., Gill, D. O., Barker, D. M., Duda, M. G., Huang, X.-Y., Wang, W., Powers, J. G.: A Description of the Advanced Research WRF Version 3. NCAR Tech. Note NCAR/TN-475+STR, 113 pp.doi:10.5065/D68S4MVH, 2008.

University of North Carolina at Chapel Hill (UNC): Operational Guidance for the Community Multiscale Air Quality (CMAQ) Modeling System Version 5.0 (February 2012 Release), available at http://www.cmaq-model.org (last access: 10 June 2020), 2012.

Visser, A. J., Boersma, K. F., Ganzeveld, L. N., Krol, M. C.: European NOx emissions in WRF-Chem derived from OMI: impacts on summertime surface ozone, Atmos. Chem. Phys., 19, 11821-11841, 2019.

Wang, N. F., Chen, Y., Hao, Q. J., Wang, H. B., Yang, F. M., Zhao, Q., Bo, Y., He, K. B., Yao, Y. G.: Seasonal variation and source analysis on water-soluble ion of $PM_{2.5}$ in Suzhou (in Chinese), Environ. Sci., 37, 4482-4489, 2016.

Wang, N., Lyu, X., Deng, X., Huang, X., Jiang, F., Ding, A.: Aggravating O_3 pollution due to NOx emission control in eastern China, Sci. Total Environ., 677, 732-744, 2019.

Wang, X., Zhang, Y., Hu, Y., Zhou, W., Lu, K., Zhong, L., Zeng, L., Shao, M., Hu, M., Russell, A. G.: Process analysis and sensitivity study of regional ozone formation over the Pearl River Delta, China, during the PRIDE-PRD2004 campaign using the CMAQ model, Atmos. Chem. Phys., 9, 635-645, 2009.

Wang, Y., Zhang, Q. Q., He, K., Zhang, Q., Chai, L.: Sulfate-nitrate-ammonium aerosols over China: response to 2000-2015 emission changes of sulfur dioxide, nitrogen oxides, and ammonia, Atmos. Chem. Phys., 13, 2635-2652, 2013.

Wei, W., Wang, S. X., Hao, J. M., Cheng, S. Y.: Trends of Chemical Speciation Profiles of Anthropogenic Volatile Organic Compounds Emissions in China, 2005-2020, Front. Env. Sci. Eng. in China, 8: 27–41, 2014.

Xing, J., Mathur, R., Pleim, J., Pouliot, G..: Observations and modeling of air quality trends over 1990–2010 across the Northern Hemisphere: China, the United States and Europe, Atmos. Chem. Phys., 15, 2723-2747, 2015.

Yang, Y., Zhao, Y.: Quantification and evaluation of atmospheric pollutant emissions from open biomass burning with multiple methods: A case study for Yangtze River Delta region, China, Atmos. Chem. Phys., 19, 327-348, 2019.

Yang, Y., Zhao, Y., Zhang, L.: Evaluating the influence of satellite observation on inversing NOx emission at regional scale. Int. Arch. Photogramm. Remote Sens. Spatial Inf. Sci., XLII-3/W9, 211–217, 2019a.

Yang Y., Zhao Y., Zhang L., Lu Y.: Evaluating the methods and influencing factors of satellite-derived estimates of NO_X emissions at regional scale: A case study for Yangtze River Delta, China. Atmos. Environ., 219, 1-12, 2019b.

Yienger, J.J., Levy, II H.: Empirical model of global soil biogenic NO_X emissions, J. Geophys. Res., 100, 11447-11464, 1995.

Zhang, Y, Bo, X, Zhao, Y, Nielsen, C.P.: Benefits of current and future policies on emission reduction from China's coal-fired power sector indicated by continuous emission monitoring, Environ. Pollut., 251: 415-424, 2019.

Zhang, Y. Y.: Characteristic of water-soluble ions in $PM_{2.5}$ in the northern suburb of Nanjing based on on-line monitoring (in Chinese), Master thesis, Nanjing University of Information Science & Technology, Nanjing, China, 2017.

Zhao, C., and Wang, Y. X.: Assimilated inversion of NOx emissions over East Asia using OMI NO_2 column measurements. Geophys. Res. Let., 2009, 36(L06805): 1-5.

Zhao, Y., Mao, P., Zhou, Y., Yang, Y., Zhang, J., Wang, S., Dong, Y., Xie, F., Yu, Y., Li, W.: Improved provincial emission inventory and speciation profiles of anthropogenic non-methane volatile organic compounds: a case study for Jiangsu, China, Atmos. Chem. Phys., 17, 7733-7756, 2017.

Zhao, Y., Yuan, M. C., Huang, X., Chen, F., Zhang, J.: Quantification and evaluation of atmospheric ammonia emissions with different methods: A case study for the Yangtze River Delta region, China, Atmos. Chem. Phys., 20, 4275-4294, 2020.

Zheng, B., Tong, D., Li, M., Liu, F., Hong, C., Geng, G., Li, H., Li, X., Peng, L., Qi, J., Yan, L., Zhang, Y., Zhao, H., Zheng, Y., He, K., and Zhang, Q.: Trends in China's anthropogenic emissions since 2010 as the consequence of clean air actions, Atmos. Chem. Phys., 18, 14095–14111, 2018.

Zhou, Y. D., Zhao, Y. D., Mao, P., Zhang, Q., Zhang, J., Qiu, L.P., Yang, Y.: Development of a high-resolution emission inventory and its evaluation and application through air quality modeling for Jiangsu Province, China, Atmos. Chem. Phys., 17, 211-233, 2017.

Zyrichidou, I., Koukouli, M.E., Balis, D., Markakis, K., Poupkou, A., Katragkou, E., Kioutsioukis, I., Melas, D., Boersma, K.F., van Roozendael, M.: Identification of surface NO_X emission sources on a regional scale using OMI NO_2, Atmos. Environ., 101, 82–93, 2015.

FIGURE CAPTIONS

Figure 1. The modeling domain and locations of meteorological and air quality monitoring sites. The map data provided by Resource and Environment Data Cloud Platform are freely available for academic use (http://www.resdc.cn/data.aspx?DATAID=201), © Institute of Geographic Sciences & Natural Resources Research, Chinese Academy of Sciences.

Figure 2. The bottom-up and top-down estimates of NO_X emissions by month for the YRD region in 2016.

Figure 3. The spatial differences between the bottom-up and top-down estimates of NO_X emissions for January, April, July and October 2016 (Top-down minus Bottom-up, mol N/s).

Figure 4. The observed and simulated hourly NO_2 concentrations based on the bottom-up and top-down NO_X emissions for January, April, July and October 2016.

Figure 5. The spatial distribution of the simulated monthly mean NO_2 concentration with the top-down estimates and differences between the simulations with the top-down and bottom-up NO_X emissions in January, April, July and October 2016 (top-down minus bottom-up).

Figure 6. The observed and simulated hourly O_3 concentrations with the bottom-up and top-down NO_X emission estimates for January, April, July and October 2016.

Figure 7. The spatial distribution of the simulated monthly mean O_3 concentration with the top-down NO_X estimates and the spatial differences between the simulations with the top-down and bottom-up NO_X emissions in January, April, July and October 2016 (top-down minus bottom-up).

Figure 8. The spatial differences between the simulated SNA concentrations with the bottom-up and top-down NO_X emission estimates for January, April, July

and October 2016 (top-down minus bottom-up).

Figure 9. The observed and simulated hourly NO_3^- concentrations with the bottom-up and top-down NO_X emission estimates for January, April, July and October 2016 at JSPEAS.

Figure 10. The spatial differences of monthly mean O_3 concentrations between the simulations based on base case (top-down estimates) and sensitivity cases in April 2016 (sensitivity case minus base case).

TABLES

Table 1. The model performance statistics of daily maximum 8-hour averaged (MDA8) O_3 concentrations in January, April, July and October 2016 with the bottom-up and top-down NO_X emissions.

Month	Emission input	Observed ($\mu g/m^3$)	Simulated ($\mu g/m^3$)	NMB	NNE
January	Bottom-up	50.6	33.0	-34.8%	38.6%
	Top-down		56.3	11.3%	27.7%
April	Bottom-up	101.5	87.2	-14.1%	20.2%
	Top-down		108.5	6.9%	16.1%
July	Bottom-up	107.4	117.3	9.2%	15.7%
	Top-down		140.7	31.0%	31.0%
October	Bottom-up	65.9	53.9	-18.3%	23.2%
	Top-down		73.4	11.3%	21.7%

Table 2. Comparison of observed and simulated NO_3^-, NH_4^+ and SO_4^{2-} concentrations by site and season in 2016 (unit: μg/m^3). The information of SNA observation sites is provided in Table S2 in the supplement. BU and TD indicate the CMAQ modeling with the bottom-up and top-down estimate of NO_X emissions, respectively.

	Spring			Summer			Autumn			Winter		
	NO_3^-	NH_4^+	SO_4^{2-}	NO_3^-	NH_4^+	SO_4^{2-}	NO_3^-	NH_4^+	SO_4^{2-}	NO_3^-	NH_4^+	SO_4^{2-}
JSPAES	19.1	16.5	12.7	5.7	9.3	10.5	10.3	6.1	9.7	31.1	16.5	20.3
CMAQ (BU)	20.7	8.5	12.0	14.4	6.0	9.1	10.9	5.0	9.0	25.6	9.3	12.8
CMAQ (TD)	22.3	9.0	12.2	11.8	5.4	9.5	11.6	5.2	9.1	26.2	9.4	12.8
SORPES	14.1	8.6	13.2	7.5	6.6	11.5	8.8	5.2	8.3	23.0	13.4	15.7
CMAQ (BU)	18.5	7.3	8.0	12.2	4.3	5.2	9.3	4.0	5.4	23.6	8.7	10.9
CMAQ (TD)	18.0	7.0	7.4	8.3	3.7	5.0	9.8	4.2	5.4	23.6	8.8	10.1
NUIST	16.9	11.0	15.9	6.8	7.1	13.1	N/A	N/A	N/A	20.9	14.3	16.8
CMAQ (BU)	20.0	7.9	9.9	14.0	5.8	7.5				24.3	9.0	11.3
CMAQ (TD)	21.8	8.5	9.9	11.8	5.3	7.8				24.6	9.1	11.3
HZS	19.9	6.6	19.9	1.9	2.8	6.2	12.7	8.3	13.3	25.3	6.6	19.5
CMAQ (BU)	14.1	5.7	8.8	5.0	1.5	2.1	8.3	3.6	6.5	18.5	6.6	9.1
CMAQ (TD)	16.0	6.3	8.6	3.7	1.3	2.8	9.3	3.9	6.6	19.9	6.8	8.9
CZS	N/A	N/A	N/A	5.1	5.1	10.9	N/A	N/A	N/A	20.4	11.8	10.9
CMAQ (BU)				11.6	4.9	7.1				23.1	9.1	11.3
CMAQ (TD)				10.7	5.0	7.3				23.1	9.1	11.3
SZS	17.8	10.2	14.7	7.9	8.0	14.9	14.2	9.0	13.1	23.2	12.5	15.1
CMAQ (BU)	14.5	6.0	7.1	13.3	5.3	7.1	6.2	2.9	6.3	19.6	7.8	11.7
CMAQ (TD)	15.5	6.3	7.1	11.7	5.0	7.7	6.9	3.0	6.3	19.9	7.9	11.7
Mean	17.6	10.6	15.3	5.8	6.5	11.2	11.5	7.1	11.1	24.0	12.5	16.4
CMAQ (BU)	17.6	7.1	9.1	11.7	4.6	6.3	8.7	3.9	6.8	22.5	8.4	11.2
CMAQ (TD)	18.7	7.4	9.1	9.7	4.3	6.7	9.4	4.1	6.8	22.9	8.5	11.0

Table 3. The changed percentages of ozone concentration based on the sensitivity analysis for April 2016.

	No reduction	-30% VOCs emissions	-60% VOCs emissions
No reduction	-	-8.9% (Case 2)	-19.5% (Case 7)
-30% NO_X emissions	14.2% (Case 1)	7.1% (Case 3)	-2.1% (Case 4)
-60% NO_X emissions	23.7% (Case 6)	19.8% (Case 5)	14.5% (Case 8)

Table 4. The changed percentages of NO_3^-, NH_4^+ and SO_4^{2-} concentrations based on the sensitivity analysis for January 2016.

	NO_3^-	NH_4^+	SO_4^{2-}	SNA
-30% NO_X emissions (Case 9)	-3.3%	-1.2%	3.8%	-1.0%
-30% NH_3 emissions (Case 10)	-16.3%	-14.5%	-0.6%	-11.7%
-30% SO_2 emissions (Case 11)	2.0%	0.2%	-2.4%	0.5%
-30% (NO_X+NH_3+SO_2) emissions (Case 12)	-15.5%	-15.5%	-4.0%	-12.4%

Figure 1.

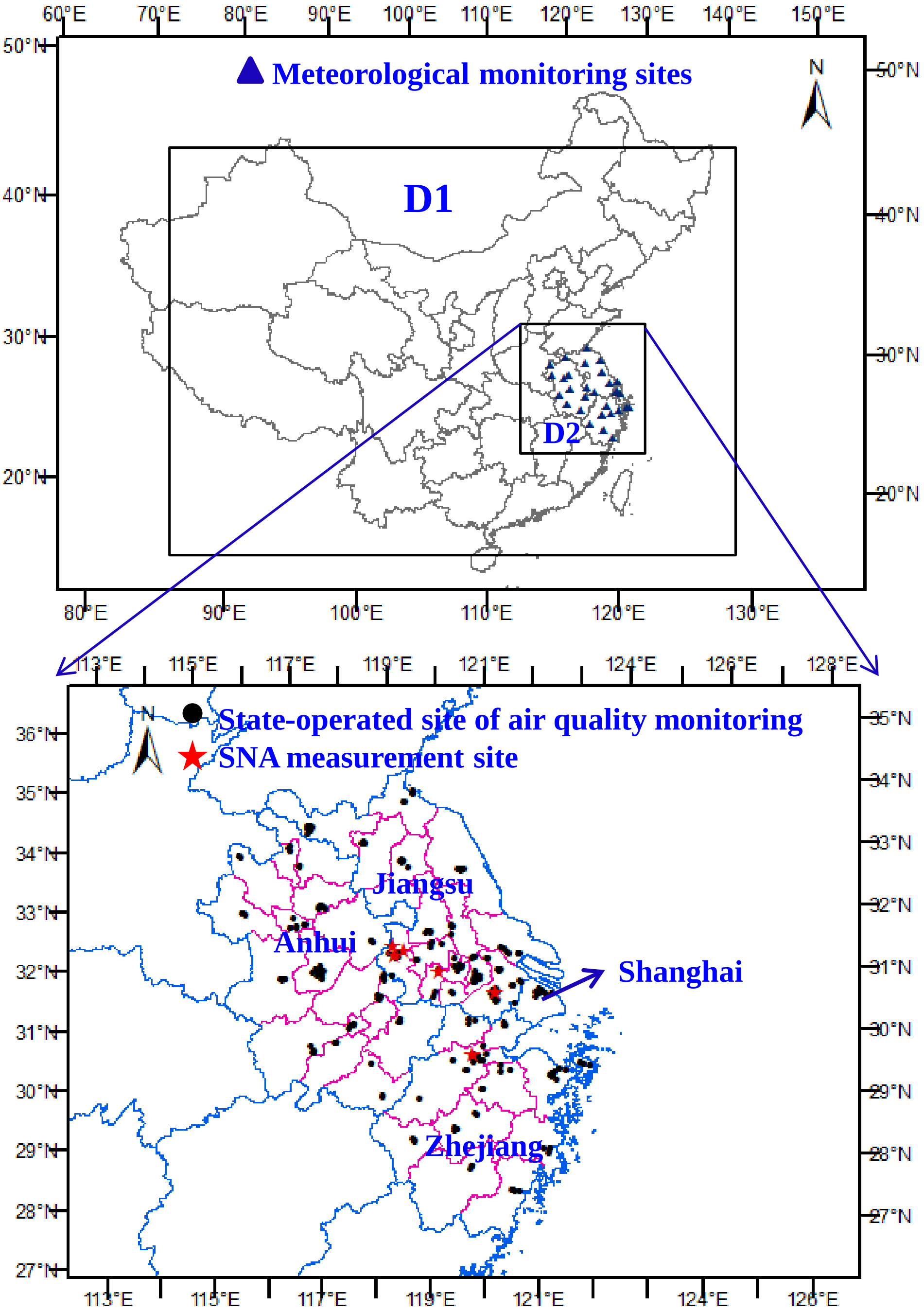
60°E
70°E
80°E
90°E
100°E
110°E
120°E
130°E
140°E
150°E
50°N
40°N
30°N
20°N
Meteorological monitoring sites
N
D1
D2
80°E
90°E
100°E
110°E
120°E
130°E
113°E
115°E
117°E
119°E
121°E
124°E
126°E
128°E
State-operated site of air quality monitoring
SNA measurement site
36°N
35°N
34°N
33°N
32°N
31°N
30°N
29°N
28°N
27°N
Jiangsu
Anhui
Shanghai
Zhejiang

Figure 2.

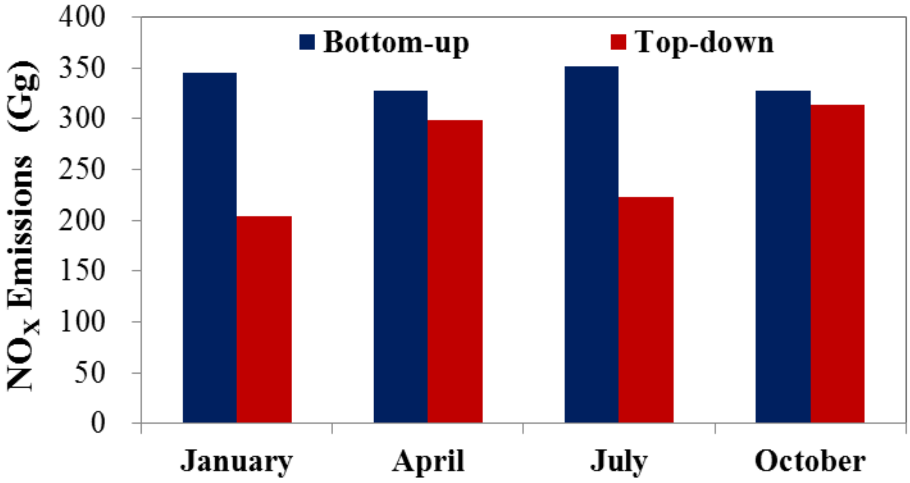

Bottom-up
Top-down
NOX Emissions (Gg)
0
50
100
150
200
250
300
350
400
January
April
July
October

Figure 3.

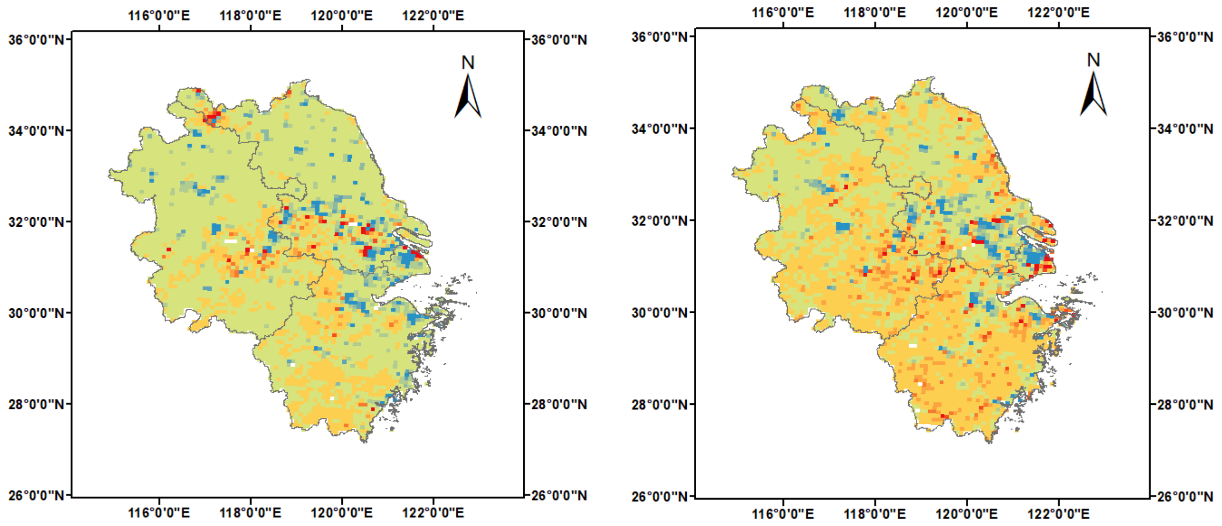

(a) January

(b) April

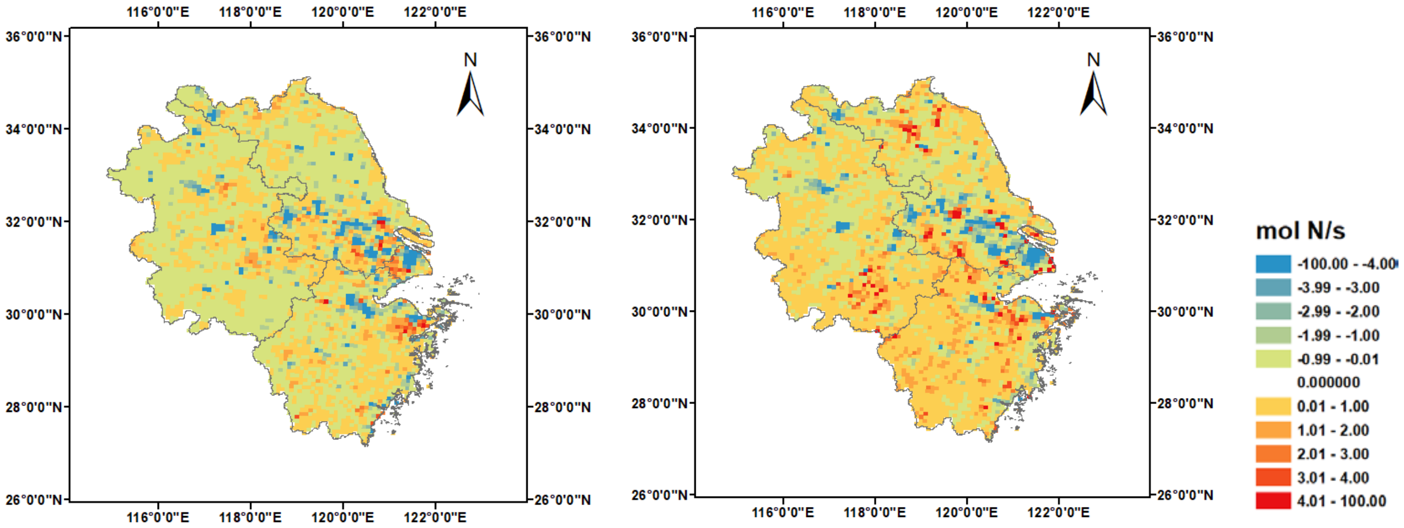

(c) July

(d) October

Figure 4.

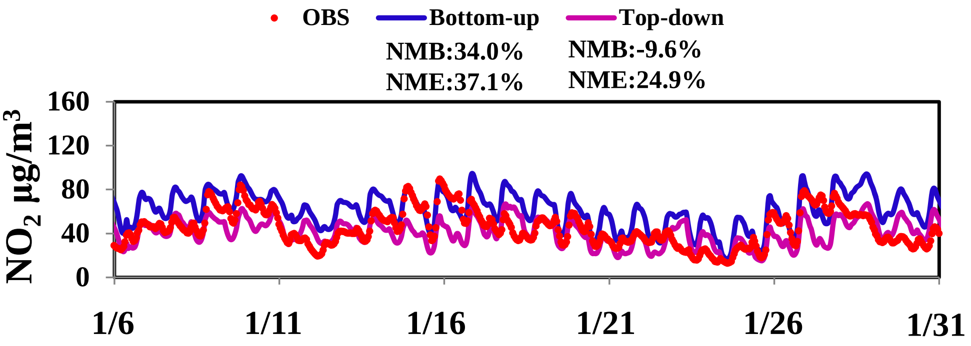

(a) January

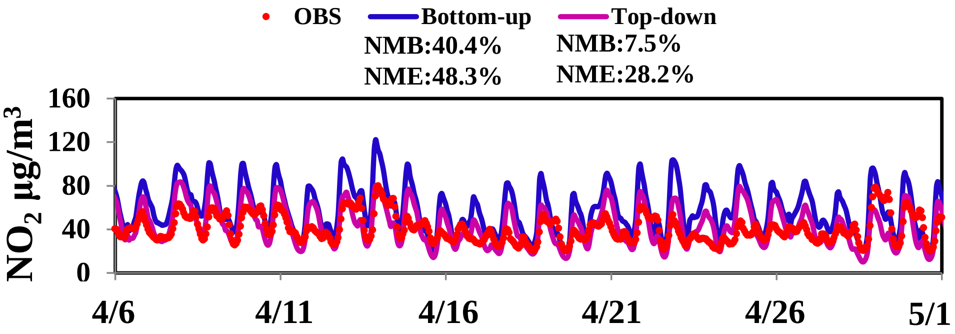

(b) April

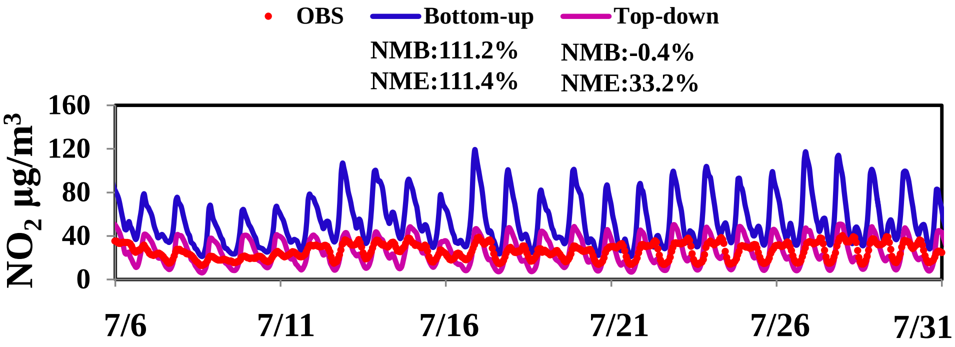

(c) July

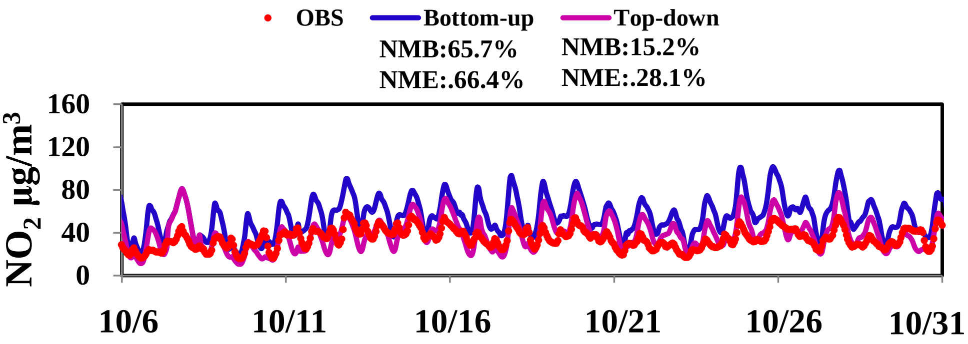

(d) October

Figure 5.

(a) January (e) January

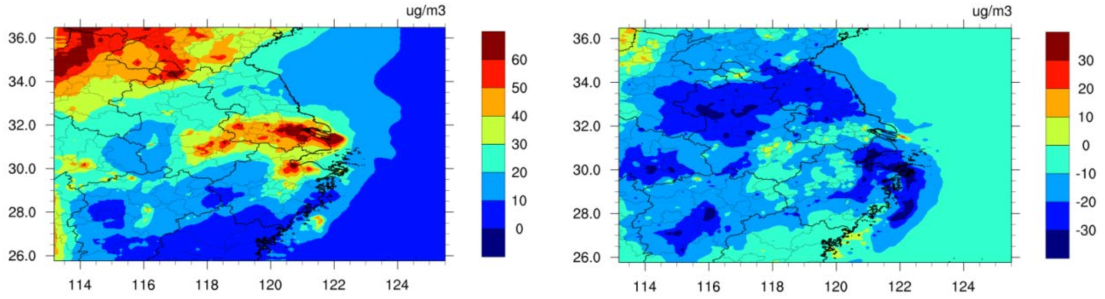

(b) April (f) April

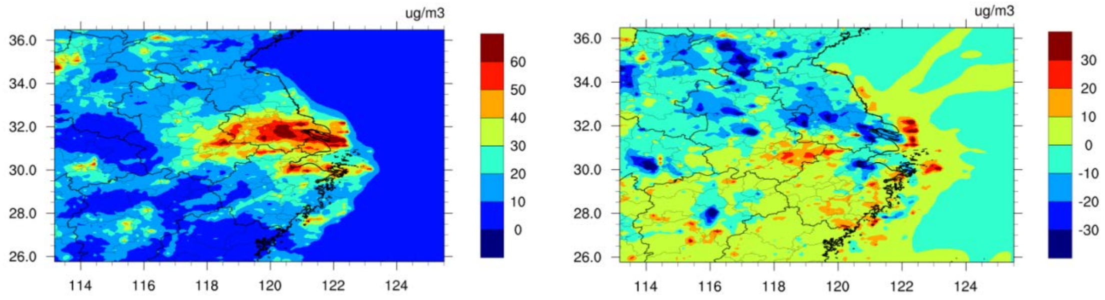

(c) July (g) July

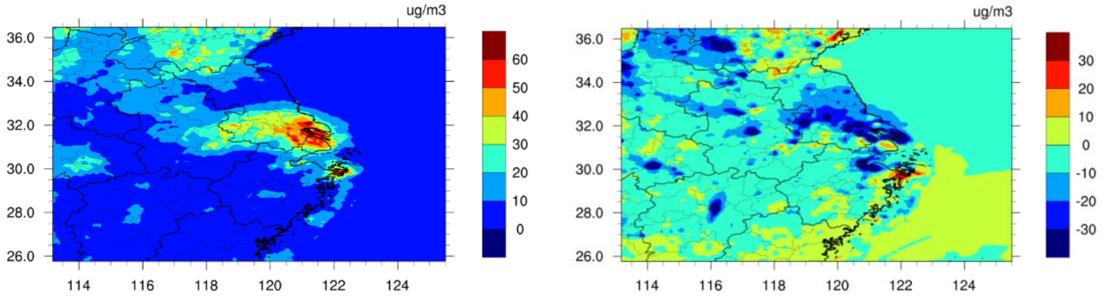

(d) October (h) October

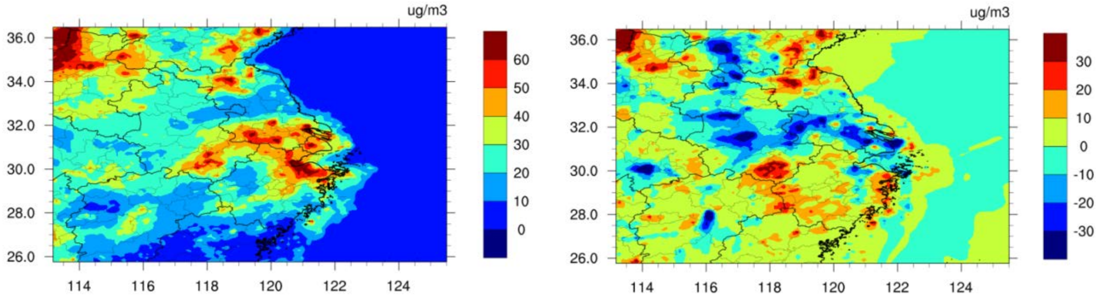

Top-down estimates Difference (Top-down minus Bottom-up)

Figure 6.

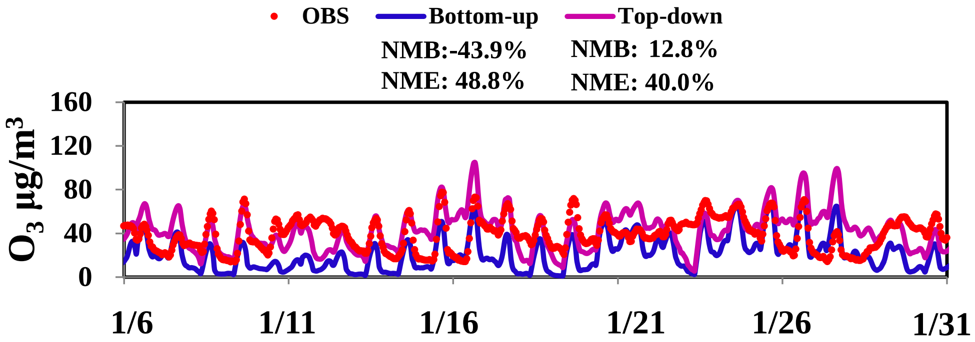

(a) January

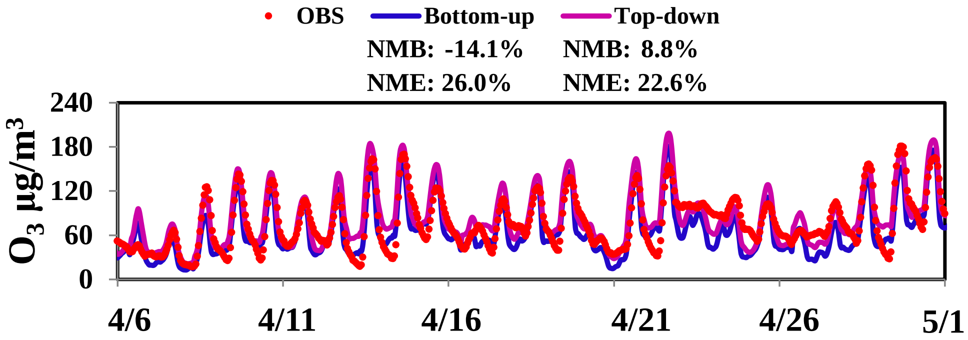

(b) April

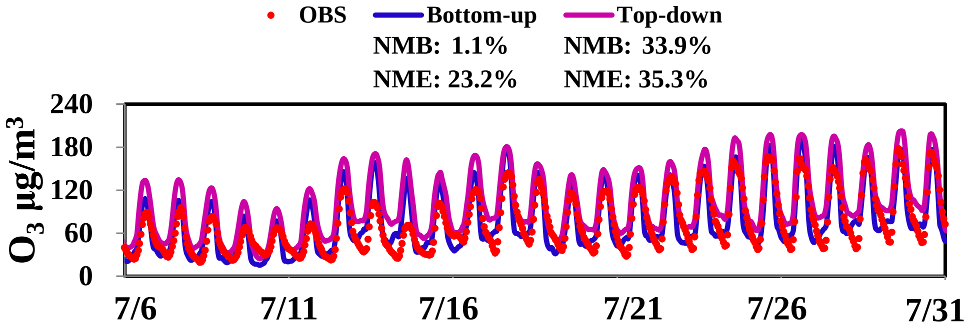

(c) July

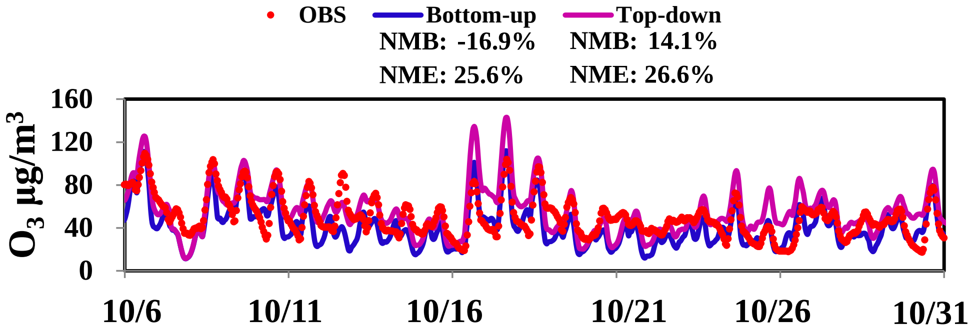

(d) October

Figure 7.

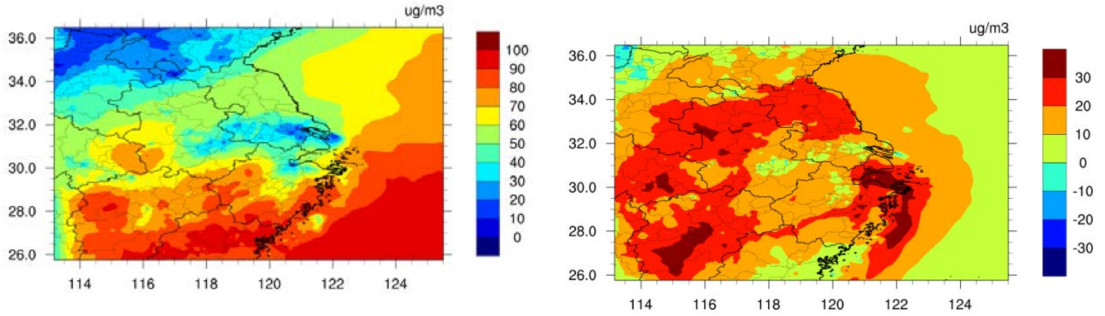

(a) January (e) January

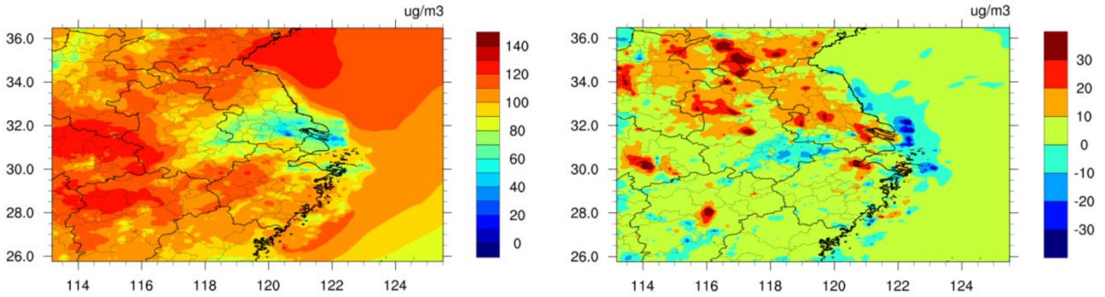

(b) April (f) April

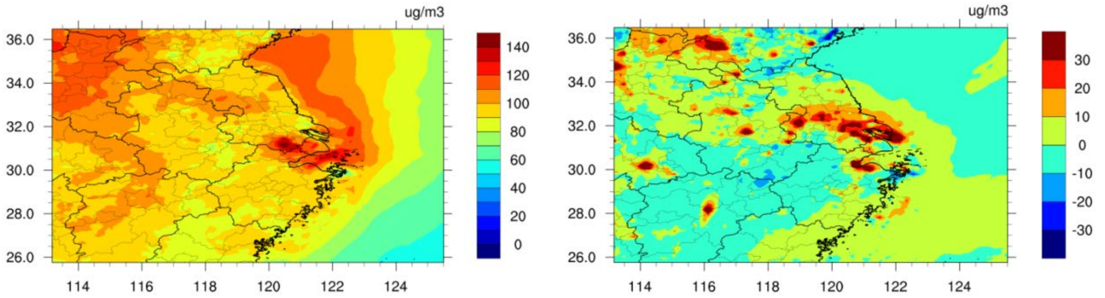

(c) July (g) July

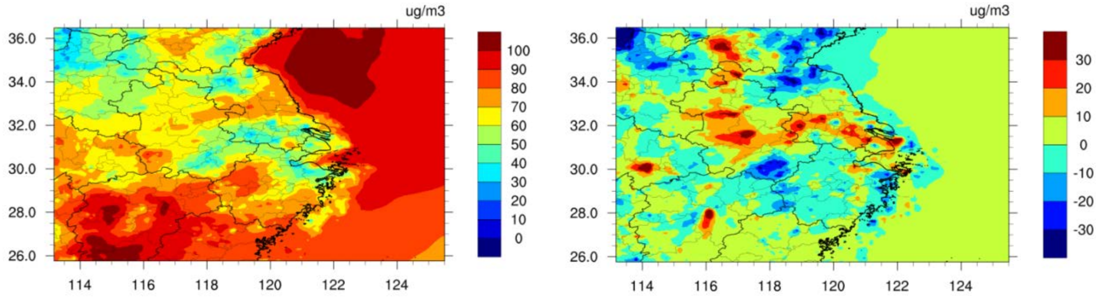

(d) October (h) October

Top-down estimates Difference (Top-down minus Bottom-up)

Figure 8.

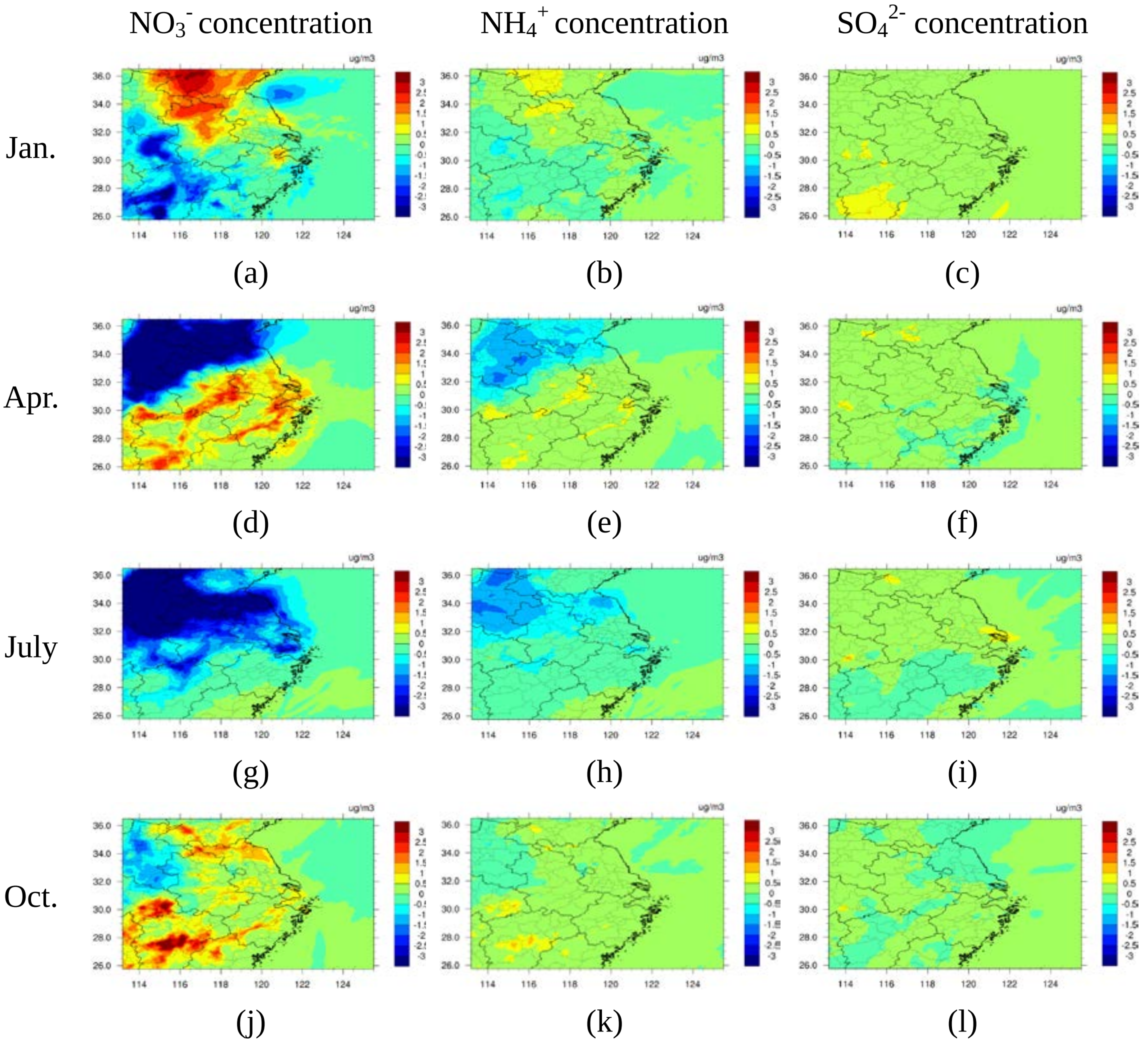
NO_3^- concentration
NH_4^+ concentration
SO_4^{2-} concentration
Jan.
Apr.
July
Oct.
(a)
(b)
(c)
(d)
(e)
(f)
(g)
(h)
(i)
(j)
(k)
(l)
ug/m3
36.0
34.0
32.0
30.0
28.0
26.0
114
116
118
120
122
124
3
2.5
2
1.5
1
0.5
0
-0.5
-1
-1.5
-2
-2.5
-3

Figure 9.

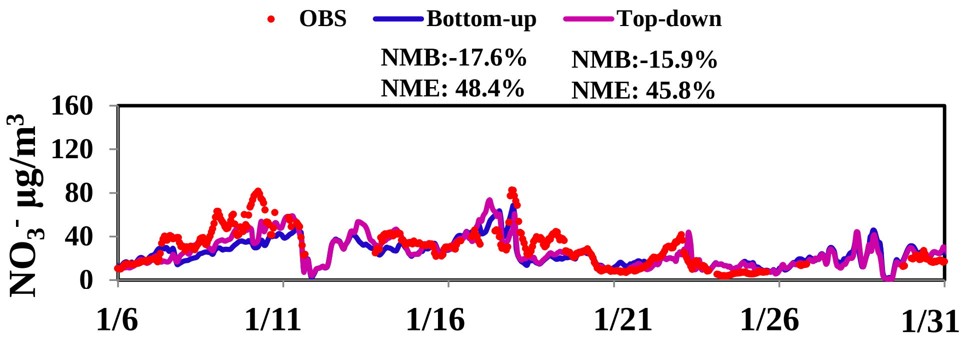

(a) January

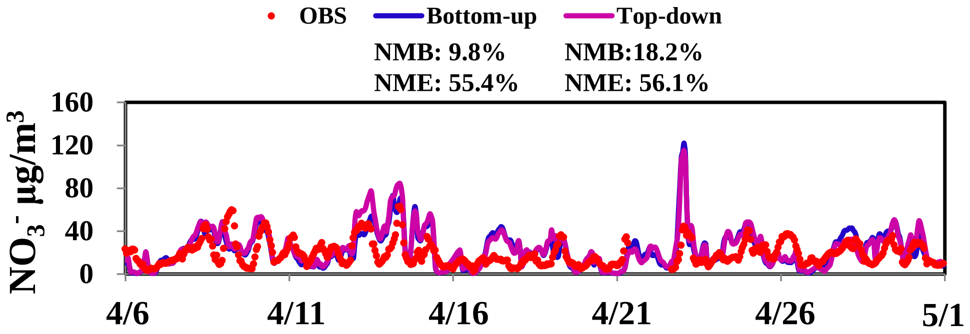

(b) April

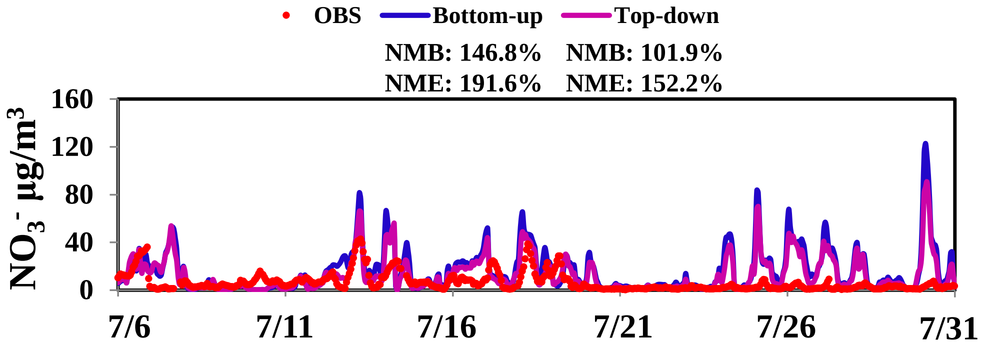

(c) July

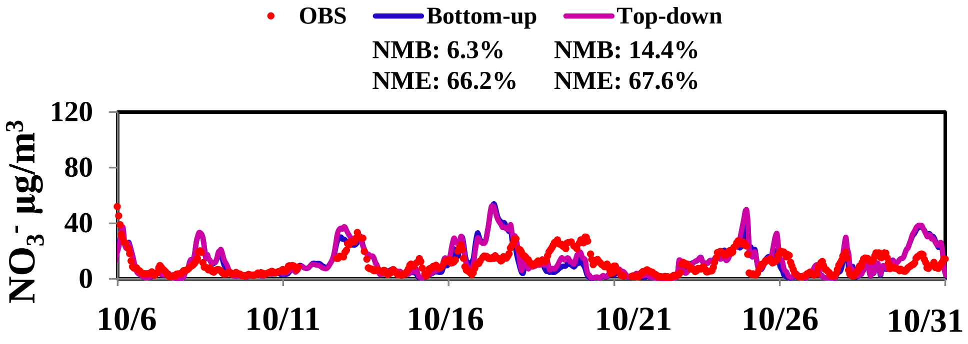

(d) October

Figure 10.

(a) -30% NO_X (b) -30% VOCs

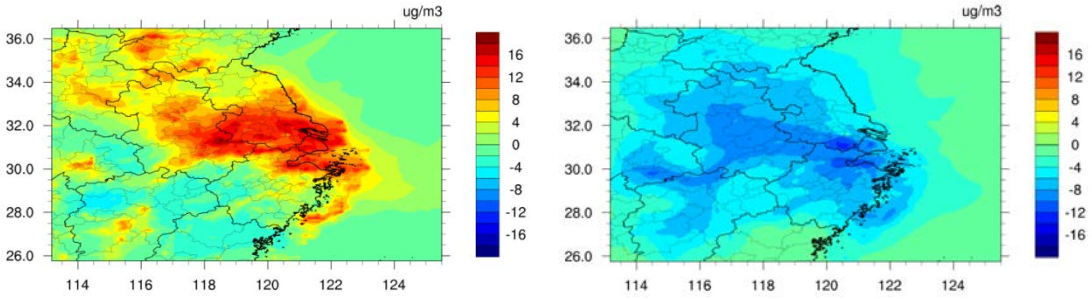

(c) -60% NOx (d) -60% VOCs

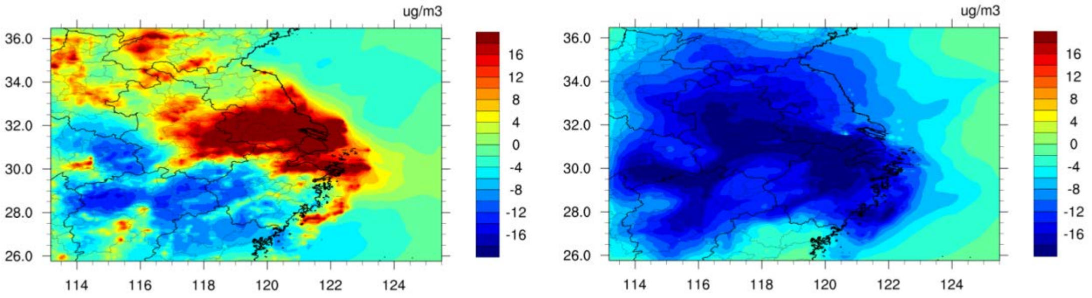

(e) -30% NO_X , -30% VOCs (f) -60% VOCs , -60% NO_X

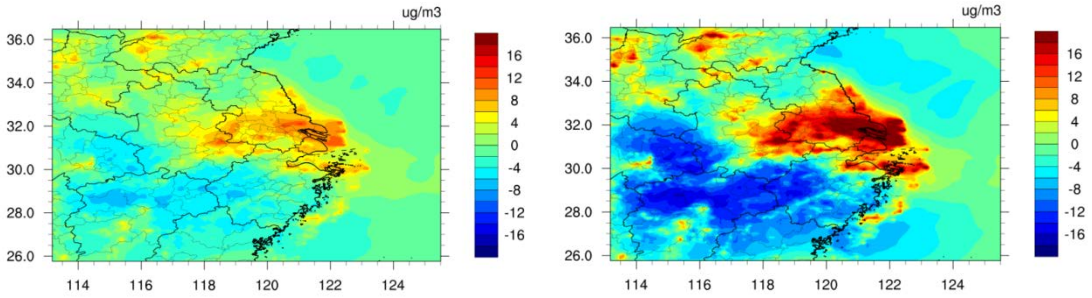

(g) -60% NO_X , -30% VOCs (h) -60% VOCs , -30% NOx